

AD-A176 926

2

# NAVAL POSTGRADUATE SCHOOL

Monterey, California



DTIC  
ELECTE  
FEB 20 1987  
S E D

## THESIS

CO<sub>2</sub> PULSED LASER DAMAGE MECHANISMS  
AND  
ASSESSMENT OF PLASMA EFFECTS (UNFOCUSED  
BEAM)

by

John S. Olson

December 1986

Thesis Advisor

F. Schwirzke

DTIC FILE COPY

Approved for public release; distribution is unlimited.

87 2 19\_002

ADA176926

REPORT DOCUMENTATION PAGE

1a REPORT SECURITY CLASSIFICATION <b>UNCLASSIFIED</b>			1b. RESTRICTIVE MARKINGS		
2a SECURITY CLASSIFICATION AUTHORITY			3 DISTRIBUTION/AVAILABILITY OF REPORT Approved for public release; distribution is unlimited.		
2b DECLASSIFICATION/DOWNGRADING SCHEDULE			4 MONITORING ORGANIZATION REPORT NUMBER(S)		
4 PERFORMING ORGANIZATION REPORT NUMBER(S)			5 MONITORING ORGANIZATION REPORT NUMBER(S)		
6a. NAME OF PERFORMING ORGANIZATION <b>Naval Postgraduate School</b>		6b OFFICE SYMBOL (if applicable) <b>33</b>		7a NAME OF MONITORING ORGANIZATION <b>Naval Postgraduate School</b>	
6c ADDRESS (City, State, and ZIP Code) <b>Monterey, California 93943-5000</b>		7b ADDRESS (City, State, and ZIP Code) <b>Monterey, California 93943-5000</b>			
8a NAME OF FUNDING/SPONSORING ORGANIZATION		8b OFFICE SYMBOL (if applicable)		9 PROCUREMENT INSTRUMENT IDENTIFICATION NUMBER	
8c ADDRESS (City, State, and ZIP Code)		10 SOURCE OF FUNDING NUMBERS			
		PROGRAM ELEMENT NO		PROJECT NO	TASK NO
					WORK UNIT ACCESSION NO
11 TITLE (Include Security Classification) <b>CO<sub>2</sub> PULSED LASER DAMAGE MECHANISMS AND ASSESSMENT OF PLASMA EFFECTS (UNFOCUSED BEAM)</b>					
12 PERSONAL AUTHOR(S) <b>Olson, John S.</b>					
13a TYPE OF REPORT <b>Master's Thesis</b>		13b TIME COVERED FROM TO		14 DATE OF REPORT (Year, Month, Day) <b>1986 December</b>	
				15 PAGE COUNT <b>86</b>	
16 SUPPLEMENTARY NOTATION					
17 COSATI CODES			18 SUBJECT TERMS (Continue on reverse if necessary and identify by block number)		
FIELD	GROUP	SUB-GROUP			
			<b>Unipolar Arcing, Laser Damage Mechanism</b>		
19 ABSTRACT (Continue on reverse if necessary and identify by block number) A theoretical study and experimental investigation of the plasma-surface interactions and laser damage mechanisms associated with the irradiation of flat, cylindrical AISI SS 304 stainless steel targets was conducted. Two experiments were accomplished, one at normal atmospheric pressure and one in a high vacuum environment, using a Carbon Dioxide transversely excited atmospheric pressure (TEA), high energy, pulsed laser with an unfocused beam to ascertain the power density threshold requirements for plasma generation. Irradiated target specimens were thoroughly examined for evidence of surface damage with a scanning electron microscope capable of clearly displaying damage features of micron size dimensions. Experimental results confirmed that surface damage was confined solely to unipolar arcing for targets irradiated with power densities near the plasma					
20 DISTRIBUTION/AVAILABILITY OF ABSTRACT <input checked="" type="checkbox"/> UNCLASSIFIED/UNLIMITED <input type="checkbox"/> SAME AS RPT <input type="checkbox"/> DTIC USERS			21 ABSTRACT SECURITY CLASSIFICATION <b>UNCLASSIFIED</b>		
22a NAME OF RESPONSIBLE INDIVIDUAL <b>Prof. F. Schwirzke</b>			22b TELEPHONE (Include Area Code) <b>408-646-2635</b>		22c OFFICE SYMBOL <b>Code 61Sw</b>

+ 01 -

Item 19. (continued)

formation thresholds. These thresholds were determined to be 0.88 Megawatts per square centimeter @ 12% at atmospheric pressure and 0.43 Megawatts per square centimeter @ 12% in the high vacuum.

A Sequential Unipolar Arcing Model, which incorporated the elaborate details of the refined Schwirzke Model, was developed to thoroughly describe the complex series of interrelated events that constitute the unipolar arcing damage mechanism. The qualitative predictions of the theoretical model were confirmed by experimental results. (Theses)

Accession For	
NTIS GSA&I	<input checked="" type="checkbox"/>
DTIC 1-5	<input checked="" type="checkbox"/>
Unannounced	<input type="checkbox"/>
Justification	
By	
Distribution/	
Availability Codes	
Dist	Avail and/or Special
A-1	



Approved for public release; distribution is unlimited.

CO<sub>2</sub> Pulsed Laser Damage Mechanisms  
and  
Assessment of Plasma Effects (Unfocused Beam)

by

John S. Olson  
Commander, United States Navy  
B.S., United States Naval Academy, 1970

Submitted in partial fulfillment of the  
requirements for the degree of

MASTER OF SCIENCE IN ENGINEERING SCIENCE

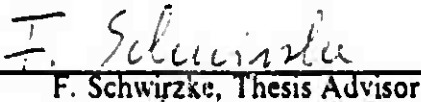
from the

NAVAL POSTGRADUATE SCHOOL  
December 1986

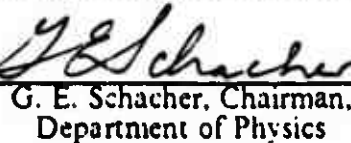
Author:

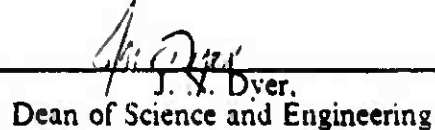
  
John S. Olson

Approved by:

  
F. Schwirzke, Thesis Advisor

  
K. E. Woehler, Second Reader

  
G. E. Schacher, Chairman,  
Department of Physics

  
J. N. Dyer,  
Dean of Science and Engineering

## ABSTRACT

A theoretical study and experimental investigation of the plasma-surface interactions and laser damage mechanisms associated with the irradiation of flat, cylindrical AISI SS 304 stainless steel targets was conducted. Two experiments were accomplished, one at normal atmospheric pressure and one in a high vacuum environment, using a Carbon Dioxide transversely excited atmospheric pressure (TEA), high energy, pulsed laser with an unfocused beam to ascertain the power density threshold requirements for plasma generation.

Irradiated target specimens were thoroughly examined for evidence of surface damage with a scanning electron microscope capable of clearly displaying damage features of micron size dimensions. Experimental results confirmed that surface damage was confined solely to unipolar arcing for targets irradiated with power densities near the plasma formation thresholds. These thresholds were determined to be 0.88 Megawatts per square centimeter  $\pm$  12% at atmospheric pressure and 0.43 Megawatts per square centimeter  $\pm$  12% in the high vacuum.

A Sequential Unipolar Arcing Model, which incorporated the elaborate details of the refined Schwirzke Model, was developed to thoroughly describe the complex series of interrelated events that constitute the unipolar arcing damage mechanism. The qualitative predictions of the theoretical model were confirmed by experimental results.

## TABLE OF CONTENTS

I.	INTRODUCTION .....	12
II.	BACKGROUND AND THEORY .....	14
	A. INTRODUCTION .....	14
	B. LASER DAMAGE MECHANISMS .....	14
	1. Sputtering .....	14
	2. Thermal Evaporation .....	16
	3. Plasma-Surface Interactions and Unipolar Arcing .....	17
III.	EXPERIMENTAL DESIGN AND RESEARCH METHODS .....	33
	A. EXPERIMENTAL APPARATUS .....	33
	1. Laser Irradiation Source .....	33
	2. Vacuum/Testing Chamber .....	35
	3. Pyroelectric Energy Meters .....	36
	4. Infrared Detector and Dewar Assembly .....	36
	5. Specialized Optical Devices .....	36
	6. Scanning Electron Microscope .....	38
	B. PROCEDURAL METHODS .....	38
	1. Laser Pulse Energy Repeatability .....	38
	2. Target Specimen Preparation .....	38
	3. Determination of Plasma Formation .....	39
	4. Evaluation of Target Surface Damage .....	41
	5. Experimental Limitations .....	41
	6. Experimental Uncertainty .....	42
IV.	EXPERIMENTAL RESULTS .....	44
	A. ONSET OF PLASMA FORMATION .....	44
	1. Plasma Formation Threshold in the Atmosphere .....	44
	2. Plasma Formation Threshold in a Vacuum .....	44
	B. TARGET SURFACE DAMAGE .....	46

1.	Unipolar Arcing in the Atmosphere .....	46
2.	Unipolar Arcing in a Vacuum .....	56
C.	DISCUSSION OF RESULTS .....	64
1.	Introduction .....	64
2.	Quantitative Comparison with Previous Results .....	64
3.	Comparison of Atmospheric and Vacuum Experiment Results .....	65
4.	Comparison of Unfocused and Focused Pulse Experimental Results .....	66
V.	CONCLUSIONS AND RECOMMENDATIONS .....	67
A.	QUALITATIVE COMPARISON OF EXPERIMENTAL RESULTS WITH THE THEORETICAL MODEL .....	67
B.	PLASMA FORMATION POWER DENSITY THRESHOLD .....	68
C.	RECOMMENDATIONS .....	68
APPENDIX A:	LUMONICS TE-822 HP CO <sub>2</sub> LASER OPERATING PROCEDURE .....	69
APPENDIX B:	TABLES .....	75
	LIST OF REFERENCES .....	82
	INITIAL DISTRIBUTION LIST .....	85

## LIST OF TABLES

1. LASER PULSE ENERGY REPEATABILITY (27 KV/7100 ENERGY METER) .....	75
2. LASER PULSE ENERGY REPEATABILITY (27 KV/3232 ENERGY METER) .....	76
3. LASER PULSE ENERGY REPEATABILITY (28 KV/7100 ENERGY METER) .....	77
4. LASER PULSE ENERGY REPEATABILITY (28 KV/7100 ENERGY METER) .....	78
5. LASER PULSE ENERGY REPEATABILITY (33 KV/7100 ENERGY METER) .....	79
6. ONSET OF PLASMA FORMATION DATA FOR SS304 TARGETS IRRADIATED IN ATMOSPHERE .....	80
7. ONSET OF PLASMA FORMATION DATA FOR SS304 TARGETS IRRADIATED IN A VACUUM .....	81

## LIST OF FIGURES

2.1	Sputtering Yields vs. Incident Energy .....	15
2.2	Reflectivity vs. Time for Stainless Steel .....	17
2.3	Plasma-Isolated Surface Interaction Prior to Cathode Spot Formation .....	21
2.4	Plasma-Isolated Surface Interaction Subsequent to Cathode Spot Formation .....	22
2.5	Unipolar Arc Model .....	23
2.6	Onset of Plasma Formation .....	24
2.7	Electric Field and Floating Potential Formation .....	26
2.8	Local Electric Field Enhancement on the Whisker Tip .....	28
3.1	Experimental Arrangement of the Laser System, Vacuum/Testing Chamber and Associated Ancillary Equipment .....	34
3.2	4.55 $\mu$ sec FWHM Pulse Width for Standard Long Pulse Gas Settings (5 $\mu$ sec per division) .....	37
4.1	Unipolar Arc Crater on Polished SS 304 Irradiated at Power Density of 1.592 MW/cm <sup>2</sup> , SEM 7110X .....	47
4.2	Unipolar Arc Crater Density Pattern on Polished SS 304 Irradiated at Power Density of 1.506 MW/cm <sup>2</sup> , SEM 1130X .....	47
4.3	Charging Spots/False Indicators of Unipolar Arcing Observed on Target No. 10, SEM 6100X .....	48
4.4	Unipolar Arc Crater Density Pattern on Polished SS 304 Irradiated at Power Density of 0.954 MW/cm <sup>2</sup> , SEM 1980X .....	50
4.5	Unipolar Arc Crater Density Pattern on Polished SS 304 Irradiated at Power Density of 1.154 MW/cm <sup>2</sup> , SEM 1440X .....	50
4.6	Small Unipolar Arc Craters on Polished SS 304 Irradiated at Power Density of 0.954 MW/cm <sup>2</sup> , SEM 12000X .....	51
4.7	Larger Well Developed Unipolar Arc Craters on Polished SS 304 Irradiated at Power Density of 1.154 MW/cm <sup>2</sup> , SEM 7920X .....	51

4.8	Unradiated Polished SS 304 Reference Target No. 18, SEM 1420X .....	52
4.9	Crater Density Pattern on Reference Target No. 18 Irradiated at Power Density of 1.578 MW/cm <sup>2</sup> , SEM 1440X .....	52
4.10	Unradiated Polished SS 304 Reference Target No. 19, SEM 1420X .....	53
4.11	Surface Damage on Reference Target No. 19 Irradiated by a Series of 6 Pulses at PRF 0.5 Hz and Average Power Density of 1.421 MW/cm <sup>2</sup> , SEM 1390X .....	54
4.12	Unipolar Arc Crater Density Pattern on Polished SS 304 Irradiated at Power Density of 0.918 MW/cm <sup>2</sup> , SEM 1390X .....	55
4.13	Unipolar Arc Crater Density Pattern on Polished SS 304 Irradiated at Power Density of 0.885 MW/cm <sup>2</sup> , SEM 2940X .....	55
4.14	Sparsely Distributed Small Unipolar Arc Craters on Polished SS 304 Irradiated at Power Density of 0.884 MW/cm <sup>2</sup> , Very Slightly Above the Plasma Formation Threshold, SEM 2940X .....	56
4.15	Unipolar Arc Crater on Polished SS 304 Irradiated at Power Density of 1.193 MW/cm <sup>2</sup> , SEM 1890X .....	57
4.16	Unipolar Arc Crater Density on Polished SS 304 Irradiated at Power Density of 1.362 MW/cm <sup>2</sup> , SEM 450X .....	58
4.17	Unipolar Arc Crater Density Pattern on Polished SS 304 Irradiated at Power Density of 0.764 MW/cm <sup>2</sup> , SEM 1400X .....	58
4.18	Unipolar Arc Crater on Polished SS 304 Irradiated at Power Density 1.008 MW/cm <sup>2</sup> , SEM 5890X .....	60
4.19	Unipolar Arc Crater on Polished SS 304 Irradiated at Power Density 0.633 MW/cm <sup>2</sup> , SEM 12,000X .....	60
4.20	Small Unipolar Arc Crater on Polished SS 304 Irradiated at Power Density of 0.480 MW/cm <sup>2</sup> , SEM 7930X .....	61
4.21	Small Unipolar Arc Crater on Polished SS 304 Irradiated at Power Density of 0.480 MW/cm <sup>2</sup> , SEM 32,800X .....	61
4.22	Unipolar Arc Crater Density Pattern on Polished SS 304 Irradiated at Power Density of 0.467 MW/cm <sup>2</sup> , SEM 1880X .....	62
4.23	Unipolar Arc Crater on Polished SS 304 Irradiated at Power Density of 0.460 MW/cm <sup>2</sup> , SEM 2870X View on Left, Topographical Confirmation on Right .....	62

4.24	Unipolar Arc Craters on Polished SS 304 Irradiated at Power Density of 0.450 MW/cm <sup>2</sup> , SEM 2870X .....	63
4.25	Unipolar Arc Crater on Polished SS 304 Irradiated at Power Density of 0.442 MW/cm <sup>2</sup> , Nearly Coincident with the Plasma Formation Threshold, SEM 2930X .....	63
A.1	Laser Pulse Energy Content Versus Laser Power Supply High Voltage Level .....	74

## ACKNOWLEDGEMENTS

I wish to thank Mr. Robert Sanders and Mr. Thomas Kellogg for their invaluable technical assistance in the CO<sub>2</sub> Laser Laboratory and on the Scanning Electron Microscope, respectively. Their unselfish efforts greatly facilitated the conduct of the experimentation and detailed analysis associated with this thesis.

The sound and timely advice and expert professional insight provided by Professor Schwirzke contributed greatly to the enjoyment and worthwhileness of this academic pursuit.

The prompt and thorough review and constructive comments offered by Professor Woehler were greatly appreciated.

To my friend and colleague Lieutenant Richard Weston, I offer my thanks for his reliable assistance during the experimental and evaluation phases of this study.

The caring support, understanding, and patience, so generously offered by my wife, Jean, and daughters, Lorry and Amanda, provided me with the best possible encouragement to successfully accomplish this demanding endeavor.

## I. INTRODUCTION

The study of laser damage mechanisms and associated plasma effects has been ongoing for a number of years, and a steadily growing interest in this scientific phenomenon has occurred coincident with the planning of various applications designed to bolster the national defense. A thorough understanding and prioritization of the damage mechanisms and the environments in which they will ultimately occur are necessary prerequisites for the successful development and future deployment of these important defensive systems. Similarly, the extensive research associated with efforts to develop a controlled nuclear fusion device, with complex plasma confinement and surface interaction design obstacles to overcome, has served to focus considerable interest on plasma effects.

During previous research conducted at the Naval Postgraduate School (NPS) using the 1.06 micron neodymium-glass laser, plasma surface interaction effects were observed on a variety of materials and surface geometries. A number of interesting plasma interaction studies have been undertaken by previous students. Brooks [Ref. 1] analyzed laser-produced plasma formation on an aluminum target from a symmetry viewpoint. A lengthy and detailed treatment of the magnetic features and electron emission characteristics of a laser-produced plasma was published by Case [Ref. 2] in 1974. The research efforts of Polk, which are documented in [Ref. 3], concentrated primarily on the laser-induced desorption of gas from stainless steel surfaces. Hwang [Ref. 4] examined the laser induced evaporation process on AISI 304 stainless steel (SS 304) targets. Keville and Lautrup [Ref. 5] analyzed the unipolar arcing damage mechanism with particular emphasis on TiC coatings.

Research on various aspects of laser produced plasma-surface effects which has been completed during the past few years by Ryan and Shedd, Hoover, Beelby and Ulrich, Metheny, Jenkins and Schmidt, and Stephenson [Refs. 6-11], has contributed to the body of knowledge currently available on this complicated subject.

The experimental data which has been collected and analyzed to date has established unipolar arcing as the dominant laser damage mechanism and has been consistent with all theoretical aspects of the Schwirzke-Taylor Unipolar Arcing Model [Ref. 12]. A detailed examination of this primary damage mechanism certainly

constitutes a worthwhile endeavor which can be reasonably expected to yield new experimental evidence leading to the reconfirmation and possible refinement of the unipolar arcing model.

The study reported herein concerned the plasma formation/unipolar arcing initiation interrelationship, plasma formation power density threshold, and the unipolar arcing laser damage mechanism. These experiments were conducted using a recently installed and activated CO<sub>2</sub> TEA (transversely excited, atmospheric pressure) high energy pulsed laser with an unfocused beam to irradiate SS 304 targets in a standard atmospheric pressure environment and also SS 304 targets contained within a vacuum chamber. A thorough examination of the arcing damage, resident at the plasma/target surface interface, was accomplished using a scanning electron microscope and optical microscope. Subsequent analysis focused on such things as crater formation and dimensions, cathode spot locations and density, and the extent of unipolar arcing damage on the metal surface. This study was conducted concurrent with comparable experimental research by Weston [Ref. 13] using a focused laser beam.

The secondary intent of this study was to clearly demonstrate the utility of the CO<sub>2</sub> TEA pulsed laser as a viable research instrument in the study of the laser damage mechanism and to thoroughly document details of its use such that future research would be both encouraged and facilitated. In this respect the comments and recommendations contained throughout this report should prove beneficial.

## II. BACKGROUND AND THEORY

### A. INTRODUCTION

The interaction of laser produced plasma with a surface has been described by a variety of theoretical models which have considered ion sputtering, thermal evaporation, and unipolar arcing as the major contributors to the damage mechanism. A basic understanding of each of these processes and their interrelationships and relative importance is a necessary prerequisite before conducting experimental research. Although some of the more subtle details of these processes are not well understood, they all are known to involve the erosion of surface material.

### B. LASER DAMAGE MECHANISMS

#### 1. Sputtering

Behrisch [Ref. 14] characterized sputtering as the bombardment of a surface with ions, neutral particles, or electrons leading to the removal of surface atoms by binary collisions which do not cause heating of the irradiated surface. A quantitative measure of this damage mechanism is expressed in terms of sputtering yield, the mean number of atoms displaced from the surface per incident bombarding particle. Sputtering yields for particles in the energy range associated with fusion research have been experimentally determined for various bombarding ions and surface materials. These investigations have shown that for light ions below a given threshold energy ( $E_{th}$ ) no sputtering occurs. Equation 2.1, which describes this relationship, is given by [Ref. 14: p. 1049]:

$$E_{th} = [1/(\gamma(\gamma-1))] U_0 \quad (\text{eqn 2.1})$$

where  $M_1 < M_2$

$\gamma = 4 M_1 M_2 / (M_1 + M_2)^2$  = Energy Transfer Factor

$M_1$  = Mass of the Incident Particle

$M_2$  = Mass of the Target Surface Atoms

and  $U_0$  = Surface Binding Energy.

Thus the threshold energy depends strongly on the incident particle target combination, and once this energy is exceeded, sputtering yield rises sharply to a maximum for incident particles in the kev energy range. The subsequent decrease in sputtering yield after attaining the peak is attributed to the increased penetration of the incident particles into the target material. Figure 2.1 illustrates these relationships for a stainless steel surface which has been subjected to bombardment by helium, deuterium, and hydrogen ions accelerated by an ion source. Curves for both single energies (dashed lines) and averaged energies assuming a Maxwellian distribution at normal incidence (solid lines) are displayed. Thus for a Maxwellian distribution of incident energies, the energy threshold for sputtering is not sharply defined, and sputtering yields at lower average energies can occur because of the higher energy particles which reside in the tail of the Maxwellian distribution. The increased sputtering yield, as a function of increased incident particle mass, is also clearly depicted in Figure 2.1 [Ref. 14: p. 1049].

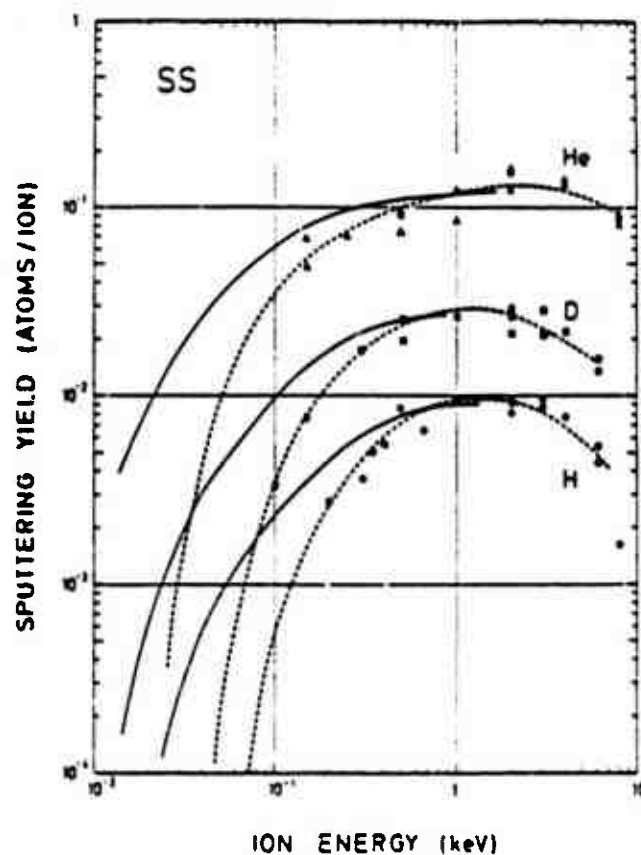


Figure 2.1 Sputtering Yields vs. Incident Energy.

The composition of the sputtered material consists primarily of neutral atoms with a wide range of energies and an angular dependence assumed to be approximately a cosine distribution [Ref. 14: p. 1050]. The significance of neutral atoms, as an integral part of the unipolar arcing initiation sequence, will be discussed in detail later in this chapter.

## 2. Thermal Evaporation

Another laser damage mechanism involves the thermal evaporation of surface material. This effect occurs when the absorbed laser energy is sufficient to heat the metal target above its vaporization point. The effectiveness of the energy coupling is a function of the target material heat characteristics, reflectivity, and the shielding effect of the laser produced plasma adjacent to the target surface on the latter portions of the incident laser pulse. Since plasma formation is known to occur within a few nanoseconds of pulse incidence, the shielding effect can be significant, particularly for longer pulse lengths. [Ref. 15]

Reflectivity, which is defined as the ratio of power reflected to incident power on the target surface, is a function of laser pulse wavelength, target material, surface finish, and the extent of surface oxidation. In general, metals with polished finishes exhibit reflectivities in excess of 0.9 when irradiated by pulses with wavelengths greater than 5 microns. Thus for the CO<sub>2</sub> TEA laser with a nominal wavelength of 10.6 microns, reflectivity is an important parameter. Since high reflectivity implies lower energy absorption, it would appear that efficient energy coupling with a metallic target would be difficult to attain. However, as shown in Figure 2.2 [Ref. 10: p. 21], it has been proven experimentally that, during the interaction of a  $1.5 \times 10^8 \text{ W/cm}^2$  pulse with a SS 304 surface, pulse widths between 100 and 600 nanoseconds produce a significant reduction in reflectivity and therefore, the effectiveness of energy coupling improves as pulse duration increases. [Ref. 15: pp. 341-343]

Since this study is concerned primarily with the interaction of an unfocused laser beam with the target surface and the determination of energy absorption thresholds for plasma formation, power densities well below those required for large scale vaporization are anticipated. Extensive vaporization effects are normally observed only near focal spot craters which have been created in a high power density environment. Although thermal evaporation effects are not expected to constitute the primary laser damage mechanism, their role in establishing conditions required for unipolar arcing is noteworthy and will be discussed later in the subsection on unipolar arcing.

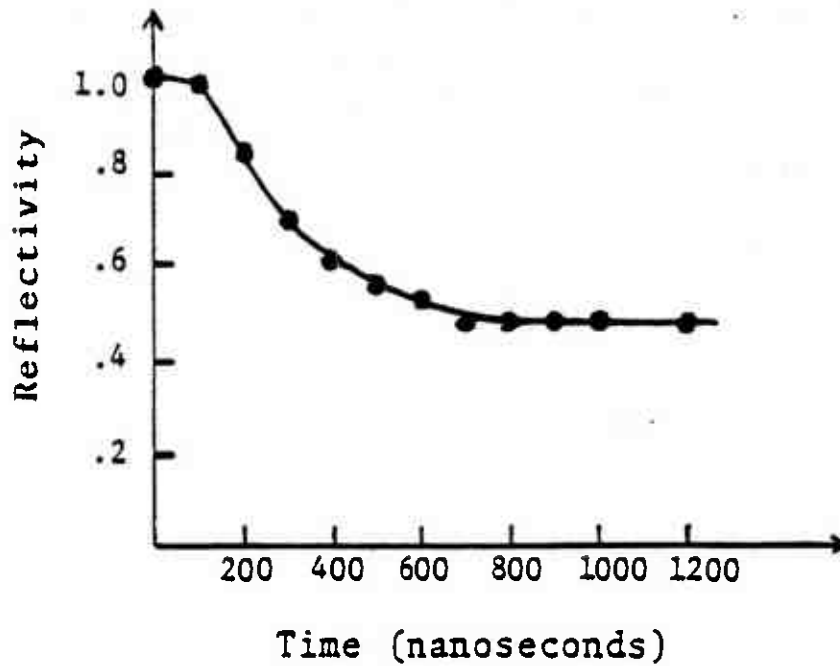


Figure 2.2 Reflectivity vs. Time for Stainless Steel.

### 3. Plasma-Surface Interactions and Unipolar Arcing

#### a. Plasma Description and Debye Shielding

Chen [Ref. 16: p. 3] defined a plasma as a quasi-neutral gas of charged and neutral particles which displays collective behavior. Quasi-neutrality implies that the electron density ( $n_e$ ) and the ion density ( $n_i$ ) are approximately equal. Collective behavior can be thought of as that feature of the plasma which describes its tendency to respond independently when subjected to outside or external influences. The ability of the plasma to effectively shield itself from applied electric potentials is quantified in terms of the Debye shielding length, which is defined by equation 2.2 (in MKS units) as [Ref. 16: p. 10]:

$$\lambda_D = (\epsilon_0 k T_e / n e^2)^{1/2} \quad (\text{eqn 2.2})$$

where

$\epsilon_0$  = Permittivity of Free Space

$k$  = Boltzmann's Constant

$T_e$  = Electron Temperature

$n$  = Plasma Density

and  $e$  = Elementary Unit of Charge.

*b. Plasma Cutoff*

One of the basic parameters used to describe a plasma is its critical density ( $n_c$ ) which is defined as the density necessary to cause the refractive index of the plasma to become zero and hence, completely reflect all incident electromagnetic waves. Since the nominal wavelength of the  $CO_2$  laser is 10.6 microns, it operates at a frequency given by equation 2.3 as:

$$f = c/\lambda = 2.83 \times 10^{13} \text{ Hz} \quad (\text{eqn 2.3})$$

where

$c$  = Speed of Light =  $3 \times 10^8$  meters/second

and  $\lambda$  = Laser Electromagnetic Wave Wavelength.

Thus the angular frequency ( $\omega$ ) of the electromagnetic wave is equal to  $2\pi f$  or  $1.778 \times 10^{14}$  radians per second. [Ref. 16: p. 120]

The relationship for the plasma frequency ( $\omega_p$ ) in radians per second is given by equation 2.4 as:

$$\omega_p = (ne^2/\epsilon_0 m_e)^{1/2} \quad (\text{eqn 2.4})$$

where  $m_e$  = Electron Mass.

After substituting the appropriate values into equation 2.4, an approximate formula that relates the plasma frequency ( $f_p$ ) and plasma density is given by equation 2.5 as [Ref. 16: p. 85]:

$$\omega_p/2\pi = f_p \sim 9n^{1/2} \quad (\text{eqn 2.5})$$

where  $n$  = Plasma Density in  $m^{-3}$ .

In a plasma which contains no magnetic field, the dispersion relation for the electromagnetic wave propagation is given by equation 2.6 [Ref. 16: p. 115]:

$$\omega^2 = (\omega_p)^2 + (ck)^2 \quad (\text{eqn 2.6})$$

where  $k$  = Wave Number.

Manipulation of equation 2.6 reveals that plasma cutoff will occur when  $\omega = \omega_p$ . This condition corresponds to a critical plasma density ( $n_c$ ) described by equation 2.7 as:

$$n_c = m_e \epsilon_0 \omega^2 / e^2. \quad (\text{eqn 2.7})$$

Substituting appropriate values for the parameters in equation 2.7,  $n_c$  for electromagnetic waves generated by the  $\text{CO}_2$  laser is found to be  $9.93 \times 10^{18}/\text{cm}^3$ . It should be noted however, that refraction effects are significant even at plasma densities as low as  $10^{16}/\text{cm}^3$  [Ref. 16: pp. 119-120].

#### *c. Plasma Sheath*

A metallic target surface in near proximity to a plasma will be struck by both positive ions and electrons. Electrons, however, have considerably greater thermal velocities than do the positive ions, and therefore, the electrons vacate the plasma at a much higher rate leaving the plasma with a net positive region and hence, a positive potential with respect to the target surface. Debye shielding causes this potential variation to be present only in a thin layer called the sheath, rather than in the entire plasma. The sheath, which is typically several Debye lengths in thickness, constitutes a potential barrier which electrostatically reflects the electrons in the plasma. The self-adjusting feature of this potential barrier ensures that the flux of electrons which possess sufficient energy to reach the surface is equivalent to the flux of positive ions, and thus quasi-neutrality is maintained. [Ref. 16: p. 290]

#### *d. Unipolar Arcing Models*

As mentioned in the introductory section of this chapter, many of the more subtle aspects of the laser damage mechanisms are not well understood. Thus, the necessity for modeling arises in order to provide reasonable explanations for scientific phenomena and a theoretical basis on which to pursue experimental verification. In

this regard a thorough review of the strengths and limitations of existing models is certainly a prudent and worthwhile endeavor.

(1) *Robson-Thonemann Model.*

Initial use of the term unipolar arc occurred in 1958 in conjunction with research by Robson and Thonemann on the behavior of an isolated metal surface in the presence of a plasma produced by gas discharge [Ref. 17]. Although the arcing process was usually thought to require a minimum of two electrodes as well as an external electromotive force, they proposed, and experimentally confirmed, a unipolar arcing mechanism which needed only a single electrode and was sustained by the thermal energy of the electrons in the plasma. As discussed earlier in the description of plasma sheath formation, the plasma maintains a positive potential with respect to the surface. This sheath potential is commonly referred to as the floating potential ( $V_f$ ) and is defined by equation 2.8 as [Ref. 18: p. 3]:

$$V_f = (kT_e/2e) \ln (M_i/2\pi m_e) \quad (\text{eqn 2.8})$$

where

$k$  = Boltzmann's Constant

$T_e$  = Electron Temperature

$e$  = Electron Charge

$M_i$  = Positive Ion Mass

and  $m_e$  = Electron Mass.

It is evident that fluctuations in the magnitude of the  $V_f$  are dependent primarily on changes in electron temperature. When plasma energy is high enough such that the electron temperature produces a  $V_f$  in excess of that necessary to initiate and maintain an arc, extensive electron emission from the cathode spot results in a lower potential called the cathode fall potential ( $V_c$ ) of the arc. Additionally, the arcing process establishes conditions which permit more electrons to return to locations on the plate which are not in close proximity to the cathode spot. These returning electrons effectively close a current loop which ensures that the quasi-neutrality of the plasma is maintained. [Ref. 17: p. 509]

Figure 2.3 [Ref. 19: p. 2] illustrates the equilibrium flow of ions and electrons from a plasma to an isolated metallic surface prior to initiation of arcing.

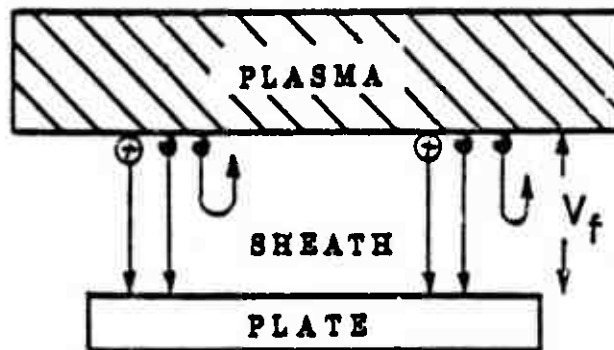


Figure 2.3 Plasma-Isolated Surface Interaction Prior to Cathode Spot Formation.

Figure 2.4 [Ref. 19: p. 2] depicts the equilibrium condition which occurs subsequent to local electron emission and commencement of unipolar arcing. These conditions generate a circulating current ( $I_c$ ) which is defined by equation 2.9 as:

$$I_c = Aen_e (kT_e/2\pi m_e)^{1/2} \times [\exp(-V_c/kT_e) - \exp(-V_f/kT_e)] \quad (\text{eqn 2.9})$$

where

$A$  = Surface Area Exposed to the Plasma

and  $m_e$  = Electron Mass.

Robson and Thonemann defined  $I_a$  as the "minimum current required to maintain the cathode spot" and indicated that its magnitude was dependent on the composition of the surface material.  $I_c > I_a$  implies that the arcing process will continue subsequent to cathode spot formation. Additionally, the Robson-Thonemann Model assumes that the electron density ( $n_e$ ) above the target surface is essentially constant and contributes to the return current over the entire area of the surface. [Ref. 17: p. 509]

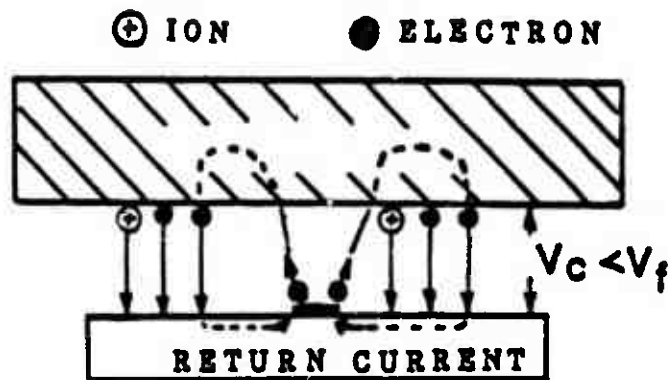


Figure 2.4 Plasma-Isolated Surface Interaction  
Subsequent to Cathode Spot Formation.

(2) *Schwirzke-Taylor Model.*

The Schwirzke-Taylor Unipolar Arcing Model extended substantially the original model of Robson and Thonemann by explaining the significance of the electric fields generated within the plasma to drive the arcing process. This model indicates that the electric field in the plasma sheath can be approximated by  $E_s \sim V_f \lambda_D$  where  $\lambda_D$  is the Debye Length. [Ref. 12: p. 780]

A series of detailed reports authored by Schwirzke and published in 1981, 1983 and 1984 further refined the model based on a thorough analysis of SS 304 targets which were irradiated by a Korad K-1500 neodymium laser operated in the Q-switched mode. Whereas the Robson-Thonemann Model implied a constant plasma density above the target surface, the refined model of Schwirzke clearly explained the necessity for an increasing plasma density above the cathode spot in order to produce an increasing electric field ( $E_{arc}$ ) and hence, promote enhanced arcing. Additionally, Schwirzke postulated the existence of a radial electric field ( $E_r$ ) which originated directly above the cathode spot because of increased plasma pressure. As clearly shown in Figure 2.5 [Ref. 20: p. 11],  $E_r$  creates a ring of reduced sheath potential which permits a greater number of electrons to return to the target surface. By following this path of opportunity through a smaller potential barrier, the electrons readily complete the unipolar arc current loop. [Ref. 19: pp. 5-6]

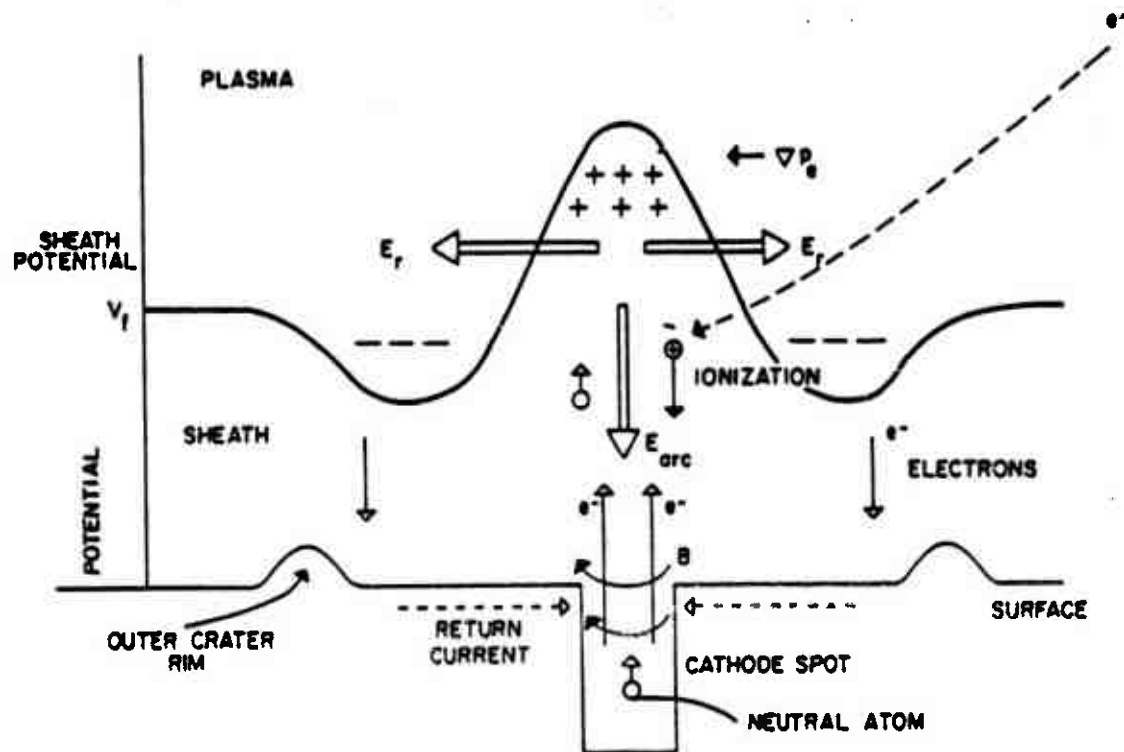


Figure 2.5 Unipolar Arc Model (Ref. 19:p. 4).

### (3) *Sequential Description of the Unipolar Arc Model.*

The unipolar arcing mechanism is comprised of a myriad of complex, interrelated processes which can be most easily comprehended when viewed from the perspective of sequentially occurring events. A model is proposed which incorporates the elaborate details of the refined Schwirzke model into a Sequential Unipolar Arc Model. This model consists of a series of rapidly occurring events which include Onset of Plasma Formation, Electric Field and Floating Potential Formation, Plasma Density Buildup, Electric Field Concentration, Enhanced Electron Emission and Whisker Vaporization, Unipolar Arc Development and the Self-Sustaining Feedback Mechanism, and Arc Cessation. These sequential events will be discussed in the succeeding paragraphs.

The initial event in this model occurs when the laser beam first strikes the target surface and is partially reflected. Absorbed energy heats the surface, and lighter surface contaminants, which are primarily gases and neutrals such as  $O_2$ ,  $CO_2$ ,

$H_2$  and  $H_2O$ , are desorbed and begin to form a weak plasma as the neutrals are ionized by energetic free electrons. Some electrons may also be ejected from the surface as a result of photoionization. At this point in the process, the magnitude of electric field, which is tangential to the target surface, is approximately zero, and thus net current at the surface is virtually nil. Figure 2.6 depicts this initial event. [Ref. 19: p. 18]

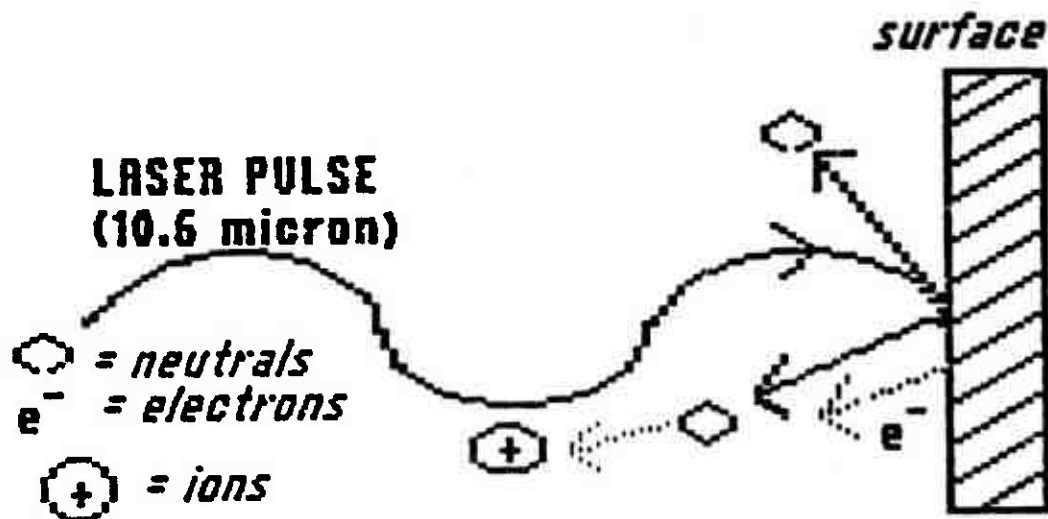


Figure 2.6 Onset of Plasma Formation.

The superposition of the normally incident and reflected laser electromagnetic waves establishes a standing wave which exhibits maximum intensity ( $I \propto E^2$ ) at a distance from the surface equal to one quarter of the wavelength ( $\lambda/4$ ) of the electromagnetic wave. The basis for determination of the maximum intensity distance is found in the relationship contained in equation 2.10, which describes the standing wave spatial intensity behavior under conditions of complete reflection for a normally incident electromagnetic wave. [Ref. 19: p. 18]

$$E^2 = 4E_0^2 \sin^2(2\pi z/\lambda) \quad (\text{eqn 2.10})$$

where

$E_0$  = E-field Magnitude

and  $z$  = Distance from Target Surface.

The free electrons within the plasma oscillate most rapidly with the electric field at  $z = \lambda/4$ . The formation of the initial plasma is most plausible at this distance from the target surface. [Ref. 19: p. 16]

Electrons, with much lower mass and much greater thermal velocity than the positive ions, quickly leave the vicinity of the positive ions, which possess lower thermal velocity, higher mass and hence, greater inertial resistance to movement. It can be seen that this leads directly to the formation of an ion rich boundary layer in the plasma which is positive with respect to the target surface. Under these conditions, a weak electric field begins to form as well as a floating potential, which has been previously defined as  $V_f$ . Quasi-neutrality is maintained in the plasma sheath by equal flow of electrons and positive ions to the surface. The relationship which is satisfied by quasi-neutrality is given by equation 2.11 as:

$$J = J_e + J_i = q_e n_e v_e + q_i n_i v_i = 0 \quad (\text{eqn 2.11})$$

where

$J$  = Current Density

$q$  = Particle Charge

$n$  = Particle Density

$v$  = Fluid Velocity

and the subscripts  $e$  and  $i$  refer to electrons and positive ions respectively. Since the plasma density is less than the critical density for cutoff, some of the incident radiation continues to reach the surface causing further damage through additional heating and desorption. As the plasma density increases, the Debye length decreases. Also a magnetic field ( $B$ ) is established by the moving particles in the plasma, however, the effect of the  $B$ -field on the unipolar arcing process at the surface has been deemed to be insignificant in comparison to the importance of the  $E$ -fields. Figure 2.7 illustrates Event 2 of the Sequential Unipolar Arc Model. [Ref. 19: pp. 18-19]

As the plasma density approaches  $n_c$ , the amount of direct laser energy incident on the target surface is progressively diminished, and increasing amounts of energy are absorbed by the plasma. The electron temperature continues to rise, and the resulting increase in the magnitude of  $V_f$  causes positive ions to be accelerated toward the surface and electrons to be more strongly reflected. Equal numbers of positive ions and electrons continue to reach the surface where they recombine, further heating the surface. The increased surface heating encourages additional desorption while the higher energy ions striking the target surface promote enhanced sputtering. Event 3 of the Sequential Unipolar Arc Model, which is called Plasma Density Buildup, has been described previously in Figure 2.3. It is influenced primarily by the increasing ionization of the neutral particles.

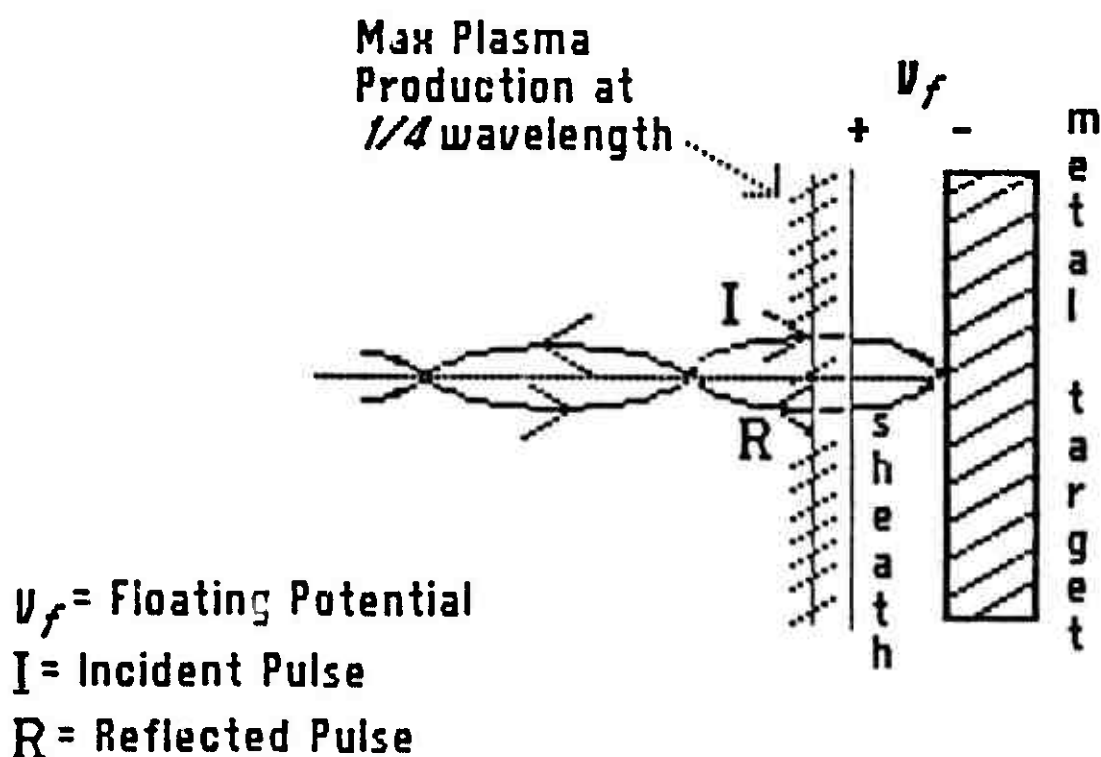


Figure 2.7 Electric Field and Floating Potential Formation.

When  $n$  reaches  $n_c$ , cutoff occurs and direct laser energy no longer reaches the target surface, but instead is partially absorbed and partially reflected by

the plasma causing both  $T_e$  and  $V_f$  to further increase.  $T_e$  however, cannot increase without bounds because inelastic collisions and the ionization process remove energy at a rate approximately equal to the rate at which the electrons absorb energy from the laser beam [Ref. 19: p. 16].

Through judicious manipulation of the equation of motion for an electron fluid and the application of simplifying assumptions, Schwirzke [Ref. 19] showed that the magnitude of the electric field in the plasma is given by equation 2.12 as:

$$E = j \cdot \sigma - \nabla P_e / n_e e \quad (\text{eqn 2.12})$$

where

$j$  = Current Density

$\sigma$  = Electrical Conductivity

and  $P_e$  = Plasma Pressure.

The simplifying assumptions included the deletion of the electron inertial term because of the relatively long time associated with arc formation ( $t \sim$  a few nanoseconds  $\gg 2\pi/\omega_{pe}$ ) and also the absence of magnetic field influences. The second term of equation 2.12 dominates, and the relationship for the electric field in the plasma can be reduced to [Ref. 19: p. 3]:

$$|E| = \nabla P_e / n_e e. \quad (\text{eqn 2.13})$$

Since  $\nabla P_e$  is equivalent to  $kT_e \nabla n$  for isothermal compression [Ref. 16: p. 67], the preceding equation may be modified as shown in equation 2.14 :

$$|E| = (kT_e / e) (\nabla n / n) \quad (\text{eqn 2.14})$$

where  $\nabla n / n = 1/d$  and  $d$  is the characteristic pressure gradient length.

Approximate magnitudes for  $kT_e$  and  $n_e$  for a weakly ionized plasma are provided by [Ref. 21: p. 40] as 10 eV and  $10^{14} \text{ cm}^{-3}$  respectively. When these values are substituted into equation 2.14 along with  $d \sim \lambda_d$ , the approximate

magnitude of the electric field within the plasma is determined to be  $3.77 \times 10^6$  V/m. The approximate relationship for the electric field in the sheath ( $E_s$ ) is given by equation 2.15 as [Ref. 19: p. 5]:

$$E_s \sim V_f \lambda_D. \quad (\text{eqn 2.15})$$

For the weakly ionized plasma parameters presented at the beginning of this paragraph,  $V_f$  and  $\lambda_D$  equal 45.2 volts and  $2.35 \times 10^{-6}$  meters respectively, and the approximate value of  $E_s$  given by equation 2.15 is  $1.92 \times 10^7$  V/m. Therefore, it is clearly evident that  $E_s$  exceeds  $E$ .

Event 4 of the Sequential Unipolar Arc Model concerns the electric field behavior near the target surface. Small surface imperfections called whiskers have been described by Miller as "microscopic surface protrusions which are typically on the order of  $10^{-4}$  cm in height with a base radius less than  $10^{-5}$  cm and a tip radius much smaller than the base radius" [Ref. 22: p. 37]. The whiskers serve as regions of electric field line concentration. This localized enhancement in electric field strength effectively focuses ion bombardment on the whisker surface causing increased sputtering of neutrals. Figure 2.8 [Ref. 22: p. 38] provides a description of the electric field concentration which constitutes Event 4.

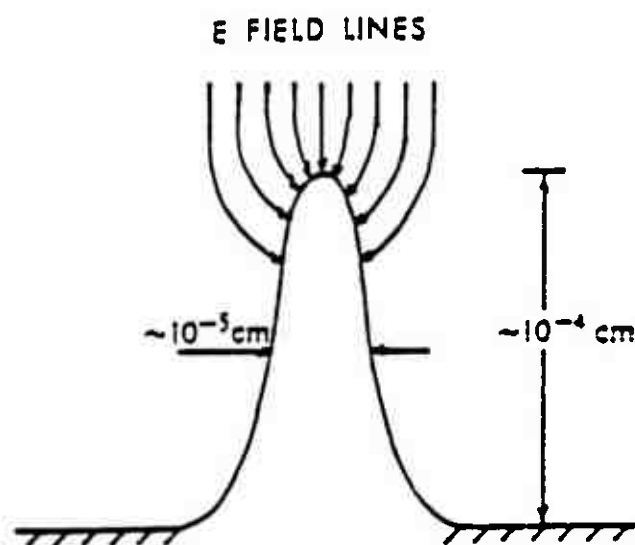


Figure 2.8 Local Electric Field Enhancement on the Whisker Tip.

As sputtering continues to increase, the density of the neutral particles available for ionization increases and results in a higher plasma density in the vicinity of the whisker. Since  $\lambda_D$  varies inversely with  $n_e$ , a rapid increase in  $n_e$  implies a rapid reduction in  $\lambda_D$ , which is accompanied by a quick rise in  $E_s$ .

In a detailed study of explosive electron emission, Parker stated that "the emission of electrons from a conducting surface affected by the presence of a strong electric field is highly dependent on the magnitude of the field and the temperature of the emitting surface" [Ref. 23: p. 17]. Event 5 of the Sequential Unipolar Arc Model, which is called Enhanced Electron Emission and Whisker Vaporization, involves the arc initiation process which relies on electron emission as its originating mechanism and occurs in an environment where the surface potential barrier for the metal electrons has been reduced by the externally generated electric field described in the preceding paragraphs. Field emission is defined as a quantum-mechanical tunneling of electrons, which have been emitted from a cold surface ( $T \sim 0^\circ \text{K}$ ), through an adjacent region of lowered potential. The threshold  $E$  for electron emission is approximately  $10^9 \text{ V/m}$  for a clean, smooth metallic surface [Ref. 23].

Comparison of the previously computed magnitude of  $E_s$  for a weakly ionized plasma with this threshold value reveals that conditions necessary for arc initiation require an enhancement of electric field strength of about 100. Halbritter [Ref. 24] has reported that enhanced electron emission from metallic surfaces occurs because of the presence of small amounts of contaminants, such as dust or hydrocarbons, and small surface protrusions. The enhanced electron emission produces gas desorption, excitation and ionization characteristic of an expanding plasma. Halbritter also indicated that field enhancement factors ranging from about 10 to 1000 could be reasonably expected and approximated the field current density ( $j_{EFE}$ ) to be  $10^7 \text{ amperes/cm}^2$ .

The voltage drop across the whisker is given by equation 2.16 as:

$$V = Ri \quad (\text{eqn 2.16})$$

where

$V$  = Voltage

$R$  = Resistance

and  $i$  = Current.

The relationship for resistance is given by equation 2.17 as:

$$R = \rho L/A \quad (\text{eqn 2.17})$$

where

$\rho$  = Resistivity

$L$  = Whisker Length

and  $A$  = Whisker Cross-Sectional Area.

The current is given by the relationship:

$$i = jA \quad (\text{eqn 2.18})$$

where  $j$  = Current Density.

Equations 2.16 through 2.18 may be combined to yield the relationship for the electric field ( $E$ ) along the length of the whisker:

$$E = V/L = \rho j_{EFE} \quad (\text{eqn 2.19})$$

By Substituting the value of  $\rho$  for SS 304 stainless steel and the approximate value for  $j_{EFE}$ , which are  $7.143 \times 10^{-6}$  ohm-cm and  $10^7$  amperes/cm<sup>2</sup> respectively, into equation 2.19,  $E$  was determined to be 7140 V/m.

When the magnitude of the enhanced electric field on the whisker tip or other surface discontinuity exceeds the required threshold, the intense electron emission which constitutes arc initiation occurs, and rapid heating of the whisker tip results in an accelerated evaporation of surface material that is often characterized as explosive. [Ref. 22: p. 38]

The relationship for the power density (MW/cm<sup>3</sup>) associated with the unipolar arcing process is given by equation 2.20 as:

$$P_v = j_{EFE} E. \quad (\text{eqn 2.20})$$

Substitution of the previously determined values of  $j_{EFE}$  and  $E$  into equation 2.20, yielded a power density of  $714 \text{ MW/cm}^3$ . In order to determine if this power density could be reasonably expected to produce whisker vaporization, the whisker heat of vaporization and volume had to be considered. By approximating the whisker geometric shape as a cylinder of base radius 0.05 microns and height 1 micron and knowing that the heat of vaporization for SS 304 stainless steel was approximately 340 kJ/mole, the total energy necessary to vaporize the whisker was calculated to be about  $1.19 \times 10^{-13}$  joules. If the whisker was assumed to be heated during the absorption of a 4.55  $\mu\text{sec}$   $\text{CO}_2$  laser pulse, the power density required to vaporize the whisker was determined to be approximately  $3.33 \text{ MW/cm}^3$ . Comparison of the two power density approximations revealed that the power density associated with the unipolar arcing process substantially exceeded the power density required to vaporize a typical whisker. Thus, the concept of explosive whisker vaporization appeared to be quite feasible.

The approximate relationship which specifies the electric field magnitude necessary to drive the arc is provided by equation 2.21:

$$|E_{\text{arc}}| \sim V_c / \lambda_D \leq V_f / \lambda_D \quad (\text{eqn 2.21})$$

where  $V_c$  is the cathode fall potential previously discussed in conjunction with the Robson-Thonemann Model. It can be readily seen that the plasma density continues to increase as more and more neutrals are being ionized, and  $\lambda_D$  continues to decrease while  $E_{\text{arc}}$  increases. Because the mean free path of electrons is greater than the sheath width, ionization of neutrals in the immediate vicinity of the arc is enhanced. These conditions lead to a further rise in plasma density, a reduction in  $\lambda_D$ , and a rapidly increasing  $E_{\text{arc}}$ . The aforementioned physical events cause increased plasma pressure above the cathode spot resulting in the creation of a radial electric field ( $E_r$ ) which, as previously discussed in the section on the Schwirzke-Taylor Model, establishes a ring of reduced sheath potential allowing more electrons to reach the target surface and close the unipolar arcing current loop. Thus, the combined effects of  $E_{\text{arc}}$  and  $E_r$  produce the feedback mechanism which propels the arc and is representative of Event 6 of the Sequential Unipolar Arc Model which is called Arc Development and the Self-Sustaining Feedback Mechanism. Events 5 and 6 are best described by Figure 2.5 which has been previously utilized to illustrate the refined Schwirzke Model. [Ref. 19: p. 5]

As the arcing process proceeds, localized cratering occurs because of the loss of surface material in the immediate vicinity of the cathode spot. A resulting increase in the plasma density causes the plasma to readily conform to the contour of the crater. Because the plasma remains adjacent to the crater and cathode spot, the feedback mechanism is maintained and cratering persists. However, as the arcing process continues, the dense plasma in the crater creates conditions which reduce the electron heat flux. This causes a decrease in electron temperature in the localized region above the cathode spot in the crater. As  $T_e$  local decreases, both the local potential and electric field strength subside. Therefore, both ionization and plasma density are reduced, and the electric field magnitude is substantially diminished. The combination of these two effects reduces the localized electric field strength until arcing can no longer be sustained. Event 7, which is called Arc Cessation, is the final event of the Sequential Unipolar Arc Model.

(4) *Discussion of Theoretical Models.*

It can be logically surmised from the preceding discussion of various unipolar arcing models that this particular laser damage mechanism is a rapidly occurring, dynamic process that depends on a complex interaction of numerous parameters, many of which are inherently variable. Although the theoretical models imply that the degree of unipolar arcing is predictable to a certain extent, they must be verified in an experimental environment where some of the parameters are held essentially constant while others are varied by known amounts. In other words, only through experimental confirmation can expected theoretical results be validated. It is with this in mind that this thesis is undertaken to investigate the effects of an unfocused laser beam-produced plasma on polished stainless steel targets at normal atmospheric pressure and in a vacuum.

### III. EXPERIMENTAL DESIGN AND RESEARCH METHODS

#### A. EXPERIMENTAL APPARATUS

The wide variety of equipment that was employed during this experimentation to irradiate SS 304 targets, produce a plasma and measure the laser beam parameters consisted of a CO<sub>2</sub> TEA high energy pulsed laser system, a testing/vacuum chamber, two pyroelectric energy meters, a low energy alignment laser, a ballistic thermopile, an infrared detector, a storage oscilloscope and various specialized optical devices designed to operate efficiently with pulses in the 10.6 micron wavelength range. A scanning electron microscope served as the primary instrument for analysis and evaluation of the laser damage mechanism on a microscopic scale. An optical microscope was also used to examine larger areas of laser induced damage on target surfaces. The overall experimental arrangement for the CO<sub>2</sub> laser, associated optical devices and energy measuring equipment, and the evacuated testing chamber is illustrated in Figure 3.1.

##### 1. Laser Irradiation Source

The Lumonics TE-822 HP high energy TEA pulsed laser [Ref. 25], was utilized to irradiate the SS 304 targets. The laser operates with an optically active medium of carbon dioxide, nitrogen and helium which flows into an optical resonator. When the gas mixture is periodically subjected to a transverse electrical discharge from the storage capacitors in the Marx generator, a population inversion occurs as a direct result of the discharge electron collisions with the CO<sub>2</sub> and N<sub>2</sub> molecules. Also, since one of the N<sub>2</sub> molecule upper vibrational levels possesses an excitation energy which is approximately equal to that of CO<sub>2</sub> molecule, the N<sub>2</sub> serves to enhance the magnitude of the population inversion by the efficient transfer of vibrational energy during collisions of the two molecules. Hence, the N<sub>2</sub> functions as a reservoir of energy which directly influences peak laser power and pulse length. [Ref. 26]

The helium is used to obtain a well diffused electrical discharge. Although the gas mixture will be heated by the discharge current flowing through it, the He removes enough of the heat to cause lower gas temperature, and therefore, depletion of the CO<sub>2</sub> upper laser level population is minimized. Additionally, relaxation of the CO<sub>2</sub> lower laser level is increased by CO<sub>2</sub>-He collisions. The presence of He allows the laser system to be pumped at higher discharge currents to produce a larger population inversion density and therefore, higher power. [Ref. 27]

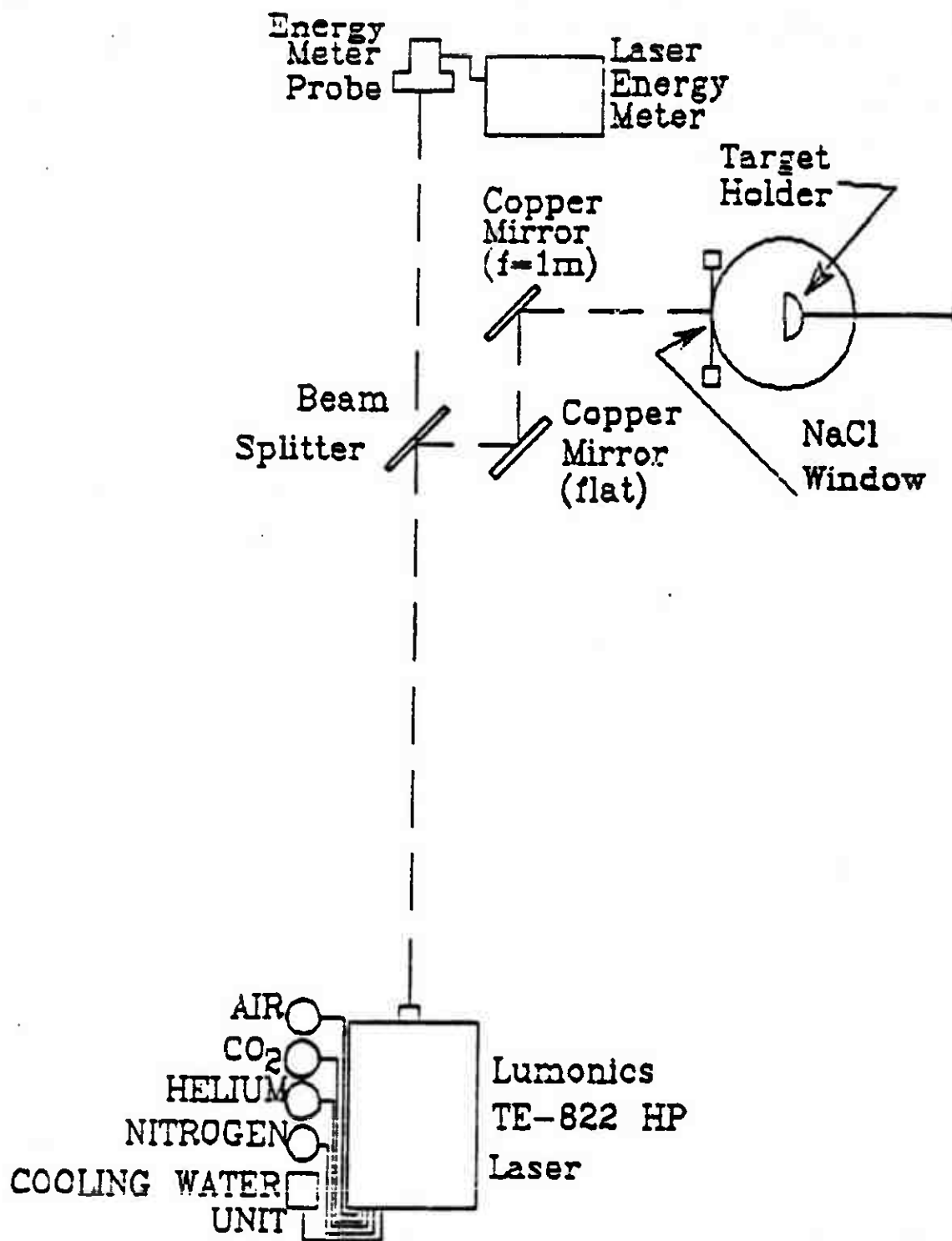


Figure 3.1 Experimental Arrangement of the Laser System, Vacuum/Testing Chamber and Associated Ancillary Equipment.

The nominal laser beam dimensions of 30 mm  $\times$  33 mm provided an approximately rectangular shape. The advertised pulse repeatability of this laser is  $\pm$  10%. During experimentation, power density was varied through a combination of high voltage settings, gas mixture proportions, and selection of appropriate optics to modify the spot size. Determination of the laser beam energy was accomplished by passing the main beam through a beam splitter and measuring its joule content with a pyroelectric energy meter.

The high voltage power supply within the laser is capable of developing up to 40 kV for charging the laser discharge capacitors. Since excessive heat buildup in this essential system component will limit its useful lifetime and quite likely cause its premature failure, measures must be taken to ensure that the high voltage power supply is continuously cooled during laser operation. The Flowrite (RPCX Mod 38) Recirculating Cooling System was employed to provide the laser system with a deionized water minimum flowrate of 25 gallons per hour in a nominal temperature range of  $20 \pm 5^\circ\text{C}$ . The cooling water system also supplied a small heat exchanger which pre-cooled the gas mixture prior to the application of the electric current discharge.

The formal laser operating procedure, which was utilized during this experimentation, and a discussion of the laser system interlocks and safety precautions are documented in Appendix A. Since Appendix A provides a sound procedural basis for the continued safe operation of the laser system and contains a graphical display of laser pulse energy versus laser power supply high voltage setting for quick and easy reference, it is strongly recommended that it be utilized by future operators.

## 2. Vacuum/Testing Chamber

The evacuated testing chamber, which was manufactured by Veeco Vacuum Systems, utilized a mechanical pump and a diffusion pump to achieve a vacuum of  $10^{-6}$  Torr. The cylindrically shaped chamber contained four entry ports. One was used for access in order to properly position target specimens. A second was used to house the target positioning and rotation device capable of holding six targets. A third contained a clear glass window for viewing events inside the chamber including polaroid camera placement for recording the light emission from irradiated target surfaces during plasma formation. The ZnSe or NaCl windows in the fourth entry port allowed the passage of 10.6 micron radiation from the optics to the target.

### 3. Pyroelectric Energy Meters

The energy content of the laser beam was measured using pyroelectric energy meters. Two different energy meters were employed during various stages of experimentation. The Rj-7100 Wide Band Energy Radiometer (serial no.603) with RjP-736 Probe (serial no. 1275) was used to measure laser beam energy content while conducting laser pulse energy repeatability studies and also while irradiating stainless steel targets. The Rk-3232 Pyroelectric Energy Meter with RkP-336 Detector Probe (serial no. RE549) was used during the laser pulse energy repeatability studies to provide comparison data and also served as the backup energy measuring device during target irradiation experiments. Both instrument/probe combinations provided system accuracies of approximately  $\pm 5\%$ . Both detector probes were designed to measure energy levels from 20 mJ to 10 J and respond favorably to pulses with 10.6 micron wavelength and durations of from less than one nanosecond to one millisecond. These instruments were operated following the guidelines specified in their respective technical manuals. [Refs. 28-29]

### 4. Infrared Detector and Dewar Assembly

An Infrared Associates, Inc. HgCdTe Infrared Detector (Mod HCT-55) and Dewar Assembly (serial no. I-4416) was utilized to measure the laser pulse shape for the recommended long pulse gas mixture. This gas mixture was obtained by adjusting all three gas regulators to 10 psi. and then establishing flow rates of 8 standard cubic feet per hour (SCFH) for carbon dioxide and nitrogen and 6 SCFH for helium. Throughout the remainder of this thesis, these flow rates will be referred to as standard long pulse gas settings. The infrared detector was operated in strict accordance with the experimental arrangement specified in its operating manual [Ref. 30]. The output signal from the detector system preamplifier was fed to a Hewlett Packard Model 468 Digital Storage Oscilloscope for analysis and photographic recording. Figure 3.2, which is a photograph of the laser pulse shape for standard long pulse gas settings, indicated that the full wave half maximum (FWHM) pulse duration was 4.55  $\mu$ sec.

### 5. Specialized Optical Devices

The optical equipment provided for use with the CO<sub>2</sub> laser installation consisted of a 3 inch diameter ZnSe beam splitter, two 3 inch diameter ZnSe windows for the vacuum testing chamber, a 3 inch diameter 300mm focal length convex copper beam expanding mirror, a 5 inch diameter 1m focal length concave copper focusing mirror, and a 4 inch diameter infinite flat focal length copper mirror. During the

course of experimentation two 3 inch diameter and one 2 inch diameter sodium chloride (NaCl) salt windows were obtained and utilized to reduce power density in the laser beam prior to incidence on the power density sensitive beam splitter. The 3 inch diameter salt windows were also used as vacuum testing chamber windows after it was determined that the ZnSe windows could not withstand the energy flux required for experimentation.

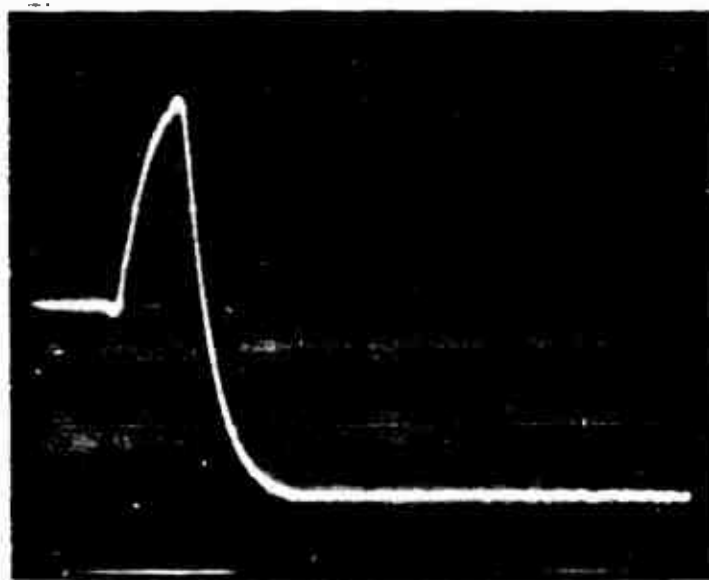


Figure 3.2 4.55  $\mu$ sec FWHM Pulse Width  
for Standard Long Pulse Gas Settings (5  $\mu$ sec per division).

Because many of the normally used optical materials such as borosilicate crown glass are opaque to the 10.6 micron wavelength produced by the  $\text{CO}_2$  laser, specialized materials must be utilized to transmit and reflect the laser beam. ZnSe is transmissive from 0.58 to 22 microns and has a refractive index of 2.4 for a 10.6 micron wavelength. NaCl has a refractive index of approximately 1.5 for 10.6 micron wavelengths and exhibits absorption varying from 8-11%. The uncoated copper mirrors provided reflectance in excess of 98.5%. [Ref. 31]

The ZnSe beam splitter was designed to reflect almost all incident laser beam energy along the path to the target while transmitting only a very small percentage of

the energy to the power density sensitive laser energy meter probe. When exposed to a 10.6 micron laser pulse, the beam splitter exhibited reflectance of 99.38%, absorption of 0.49% and transmittance of 0.13%. These characteristics enabled the laser power meter probes to be operated in most cases at power density levels well below their damage threshold of approximately 1 MW/cm<sup>2</sup>.

#### **6. Scanning Electron Microscope**

The Cambridge Stereoscan 200 Scanning Electron Microscope (SEM) was the primary analysis instrument used for the detailed evaluation of surface damage on irradiated targets. It provided a full range of magnifications from 30X to 300,000X and excellent resolution which allowed examination and photography of laser damage features in the 1 micron diameter range. The SEM was essential for the study and accurate recording of minute unipolar arc crater features and for crater density approximations. [Ref. 32]

### **B. PROCEDURAL METHODS**

#### **1. Laser Pulse Energy Repeatability**

Because the CO<sub>2</sub> laser installation had not been thoroughly tested prior to the start of this experimentation, a moderate amount of laser system testing was required prior to commencing laser damage mechanism research. Control of the laser beam energy was essential to maintaining power densities within close tolerances in order to protect sensitive optics and energy meter probes as well as to facilitate the determination of power density thresholds for onset of plasma formation. Therefore, laser pulse energy repeatability studies were conducted at representative laser system settings to ascertain the extent to which laser beam energy could be controlled. A series of 45 laser shots were made through the beam splitter and measured using both of the previously described laser energy meters. The results of this testing revealed that laser pulse energy repeatability varied in a range from  $\pm 1.26\%$  to  $\pm 1.94\%$ . Tables 1-5, which document these test results, are included to serve as a baseline reference to which future CO<sub>2</sub> operators may refer to quickly assess the laser system controllability performance.

#### **2. Target Specimen Preparation**

SS 304 targets were machined from bar stock to a flat cylindrical shape with dimensions of 0.5 inch diameter and 0.125 inch height. Individual targets were mounted in bakelite holders to facilitate mechanical polishing. Mechanical polishing

was accomplished using progressively finer  $\text{Al}_2\text{O}_3$  slurries. During the final stage of polishing, a 0.05 micron  $\text{Al}_2\text{O}_3$  slurry was used. Polished targets were cleaned with deionized water, thoroughly dried, and placed in a desiccant chamber until needed for experimentation. Targets required for each experiment were carefully removed from their bakelite holders, cleaned with deionized water and ethanol, and dried with nitrogen prior to being mounted in the target holder for irradiation by the laser beam.

Irradiated targets were immediately mounted on stubs, suitable for use in the scanning electron microscope, with either silver paint or colloidal graphite. SEM analysis of targets was scheduled as closely as possible to the actual irradiation of the targets to minimize the deterioration of the target surface due to oxidation. In instances where the SEM could not be immediately utilized to evaluate target damage, irradiated targets were stored for short periods in the desiccant chamber.

### 3. Determination of Plasma Formation

#### a. Onset of Plasma Formation in Atmosphere

Plasma formation onset was determined by varying the laser beam power density through a combination of spot size and laser beam energy adjustments. Spot size was varied by target location. Spot size at a given target location was measured on recording paper prior to irradiating the target. The energy content of the laser beam was controlled by adjusting the high voltage power supply setting. Subsequent to completion of a careful optical alignment using the low energy alignment laser and determination of the correct spot size, beam energy combination necessary to yield the desired power density, the target was irradiated. The laser beam was reflected via the beam splitter and the 1 meter focal length copper mirror to the target. The beam energy, transmitted by the beam splitter, was routed to the pyroelectric energy probe, and the energy level was recorded on the laser power meter.

The power density incident on the target surface was determined by considering the spot size, laser energy meter reading, adjustment for the beam splitter optical characteristics, and absorption losses. Equation 3.1, which allows the determination of power density at the target surface, is given by:

$$P_d = E R_b R_m T_b A t \quad (\text{eqn 3.1})$$

where

$P_d$  = Power Density at the Target Surface in watts  $\text{cm}^{-2}$

$E$  = Reading on the Laser Energy Meter in joules

$R_b$  = Beam Splitter Reflectance = 0.9938

$R_m$  = Copper Mirror Reflectance (worst case) = 0.985

$T_b$  = Beam Splitter Transmittance = 0.0013

$A$  = Beam Spot Size in  $\text{cm}^2$

and  $t$  = FWHM Laser Pulse Duration in seconds = 4.55 microseconds.

Experimental irradiation of the SS 304 targets was conducted in a darkened laboratory so that a polaroid camera, with the shutter held open during the laser shot, could be utilized to provide a photographic record of the emitted light associated with plasma formation.

*b. Onset of Plasma Formation in a Vacuum*

The procedure employed for this experiment was an expanded version of the procedure used for irradiation of targets in atmosphere. Irradiation of SS 304 targets within the vacuum/testing chamber required the addition of a second copper mirror (as shown in Figure 3.1) in order to bring the laser beam through the power density sensitive ZnSe chamber window with a spot size sufficiently large so that window damage did not occur. Although the spot size incident at the chamber window was relatively large, spot size at the target surface was required to be considerably smaller to ensure that power densities were high enough to initiate plasma formation. Thus, painstakingly careful optical alignment was required prior to each laser shot. This was accomplished using a beam expander in conjunction with the low energy alignment laser to thoroughly analyze spot sizes and beam shape distortions associated with the placement of the optical devices, particularly the copper mirrors. Subsequent to completion of the optical alignment, laser test shots were made to actually measure spot size at the chamber window and at the target surface position. Only when this procedure revealed compatibility of spot sizes at both locations was target irradiation conducted.

The SS 304 targets were then carefully positioned in the vacuum testing chamber, the chamber resealed, and a vacuum of at least  $10^{-6}$  torr was verified. The laboratory was darkened, and a polaroid camera, with its shutter held open, was positioned adjacent to the chamber viewing window for recording evidence of plasma

formation. A small portion of the laser beam energy was transmitted to the pyroelectric energy probe and recorded on the laser energy meter.

Power density incident at the target surface was computed using equation 3.1 after modifying it to include a second factor of 0.985 for reflectance of the additional copper mirror and the transmittance value for the vacuum chamber window.

#### 4. Evaluation of Target Surface Damage

All irradiated SS 304 targets were prepared for SEM evaluation as previously described in the subsection on target specimen preparation. The capability provided by the SEM to examine and photograph damage features with dimensions in the 1 micron range greatly enhanced the evaluation efforts. Additionally, the electron back scatter analyzer supported the topographical evaluation of the target surfaces. This was particularly significant for targets irradiated near plasma formation thresholds which did not always exhibit well formed and clearly distinguishable crater rims. Topographical analysis facilitated the differentiation between darkened surface areas and surface holes indicative of the presence of craters.

#### 5. Experimental Limitations

##### *a. Laser Pulse Energy Distribution and Beam Shape Nonuniformities*

Because of the lack of an unstable resonator as part of the CO<sub>2</sub> Laser Facility experimental apparatus, generation of a pure Gaussian pulse shape was not possible. Although the beam shape remained consistent throughout the experimentation, its energy distribution pattern was only approximately uniform and did contain a few areas of higher energy densities commonly referred to as hot spots. Due to these nonuniformities, a degree of uncertainty, conservatively estimated to be about  $\pm 10\%$ , was encountered.

##### *b. Laser Pulse Duration*

A laser pulse duration of 4.55  $\mu\text{sec}$  was directed to be used throughout the experimentation in order to limit the peak energy in the pulse and protect the sensitive optics from unnecessary exposure to high energy fluxes. Although a detailed study of laser damage mechanism dependence on pulse width was unable to be accomplished, comparison of experimental results with previous results obtained with a neodymium laser of shorter pulse duration was made.

##### *c. ZnSe Vacuum Chamber Window*

Premature failure of the ZnSe vacuum chamber window, at a power density much lower than the expected damage threshold, required the utilization of NaCl salt

windows in the vacuum chamber. The significance of this limitation will be discussed in detail in the chapter on experimental results.

*d. Target Orientation*

In order to prevent reflection of the laser pulse from the target surface back along the optical path to the laser internal optics, target surfaces were canted 3-5 degrees away from perpendicular incidence. This procedural measure was invoked so that the potential for catastrophic damage to the laser could be effectively precluded. Although this meant that the exact normal incidence assumed in the theoretical model could not be perfectly achieved, the  $\lambda/4$  relationship for the distance of maximum intensity was still closely approximated by the experimental arrangement. Additionally, the  $\lambda/4$  factor was used only as a representative distance for the calculation of the approximate electric field magnitude in the plasma. This experimental limitation was considered to be of minor significance.

*e. Laser Cooling Water Unit*

The Flowrite Recirculating Cooling System malfunctioned on 6 occasions during the course of experimentation and was out of commission an average of 1-2 days per occurrence. Since the CO<sub>2</sub> laser system could not be operated during these periods, significant delays in experimentation were encountered.

*f. Vacuum Chamber Mechanical Pump Exhaust*

During pre-experimentation testing of the vacuum chamber, it was noted that the mechanical pump exhaust filtering was inadequate and that moderate amounts of oily smoke leaked into the experiment area enclosure. Before experimentation was commenced, the enclosure area was thoroughly cleaned and a temporary exhaust line was installed to remove exhaust from the enclosure to prevent contamination of the delicate optics. Thus this experimental limitation was removed before it could adversely effect experimental results.

**6. Experimental Uncertainty**

A thorough assessment of experimental errors was necessary in order to characterize the accuracy of subsequent experimental results. Therefore, the identification of potential errors and their expected magnitudes was an essential feature of the analysis process.

As discussed earlier in this chapter, laser pulse energy distribution nonuniformities and laser energy meter inaccuracies contributed estimated uncertainties of  $\pm 10\%$  and  $\pm 5\%$  respectively. These sources of potential error were considered the most significant of those encountered during the experiment.

Other potential error sources of lesser significance included laser spot size measurement, optical devices transmittance and reflectance inaccuracies, and NaCl window calibration. Uncertainty attributed to each of these sources was estimated to be  $\pm 2\%$ .

Assuming an unlikely worst case in which all of the estimated errors were additive, a total uncertainty of approximately  $\pm 18\%$  would be expected. If, on the other hand, it was assumed that each potential error source was independent of all other sources, an uncertainty analysis method outlined by Holman [Ref. 33] may be utilized to determine a more reasonable magnitude for the total expected error. Holman used the following relationship to assess the combined effects of a group of independent uncertainties:

$$U_{\text{tot}} = [U_1^2 + U_2^2 + U_3^2 + \dots]^{1/2} \quad (\text{eqn 3.2})$$

where

$U_{\text{tot}}$  = Total Expected Uncertainty

and  $U_n$  = Independent Uncertainties.

Substituting the values for the individual uncertainties into equation 3.2 yields an estimated combined uncertainty of  $\pm 11.7\%$ . A similar calculation for the atmospheric experiment, which did not require a calibrated NaCl window, yielded a slightly lower estimated composite experimental error of  $\pm 11.5\%$ .

In view of the preceding analysis, a composite experimental error conservatively estimated to be  $\pm 12\%$  was chosen for both the atmospheric and vacuum experiments.

## IV. EXPERIMENTAL RESULTS

### A. ONSET OF PLASMA FORMATION

#### 1. Plasma Formation Threshold in the Atmosphere

A total of 27 SS 304 stainless steel targets were irradiated in the atmosphere with relatively low power and an unfocused beam in order to ascertain the power density threshold for plasma formation. The first five targets were subjected to power densities in the 1.5-2.2 MW/cm<sup>2</sup> range and clearly exhibited plasma formation. Targets 6 through 13 were irradiated at power densities ranging from 0.051 to 0.527 MW/cm<sup>2</sup> but failed to display any indication of plasma formation. After bracketing the power density range required for initiation of plasma formation with the first two series of target specimens, the remaining 14 shots were conducted in a narrower range of power densities from 0.65 to 1.5 MW/cm<sup>2</sup>. Irradiation of Targets 13-20 revealed that plasma formation onset occurred in the 0.72-0.95 MW/cm<sup>2</sup> power density region. These results supported continued experimentation with a further reduced range of power densities from 0.79-0.95 MW/cm<sup>2</sup>, and thus, the final 7 targets in the series were utilized to establish the expected range of power densities at which plasma formation could be reasonably expected to occur. The results of this experiment are summarized in Table 6.

On the basis of the aforementioned experimental data and allowing for inaccuracies because of hot spots in the nonuniform laser beam and for procedural and equipment accuracy limitations, a plasma formation power density threshold range of 0.88 MW/cm<sup>2</sup>  $\pm$  12% was selected.

#### 2. Plasma Formation Threshold in a Vacuum

A total of 27 SS 304 stainless steel targets were irradiated in a vacuum of approximately 10<sup>-6</sup> torr using an unfocused pulse with relatively low energy content to determine the power density threshold for plasma formation.

Targets 28 and 29 were irradiated with a nominal beam size of 33mm by 30mm using the beam splitter to reflect the laser pulse through the ZnSe vacuum chamber window to the target surfaces. Although a report of previous experimentation with ZnSe had confirmed its ability to withstand laser pulse energy levels in the 27-41 joules.cm<sup>2</sup> range for a 600 nanosecond pulse duration [Ref. 15: p. 153], window

breakdown due to thermal runaway had previously occurred during testing of the vacuum chamber at an energy density of approximately 20 joules/cm<sup>2</sup>, well below its expected damage threshold. Because of preferential absorption in the area of previous damage, a reliable and accurate measurement of uniform window absorption was unable to be accomplished, and the data obtained from irradiation of Targets 28 and 29 was of approximately order of magnitude quality only. Examination of the ZnSe window, subsequent to irradiation of these targets with laser pulse energies below 4 joules/cm<sup>2</sup>, revealed additional small thermal breakdown marks on the window surface. The inability to utilize the ZnSe vacuum chamber window, provided for use with the CO<sub>2</sub> laser installation because of its supposedly very low energy absorption and excellent transmittance, constituted an experimental equipment limitation. The ZnSe window was replaced with a NaCl window for the remainder of the vacuum experiment. Initial calibration of the salt window indicated a transmittance of 0.891. Utilization of the salt window required a modification of procedures to include provisions for the careful installation and calibration of the window, the use of a heat lamp adjacent to the window to minimize the detrimental effects of humidity and resultant window fogging, removal and storage of the window in a nitrogen bag within a desiccant chamber during periods between use, and periodic repolishing of the salt window to maintain its optical and energy transmittance characteristics. Although additional time and effort were required to conduct these expanded procedural requirements, the salt window's excellent performance throughout the remainder of the experiment at energy densities up to 7 joules/cm<sup>2</sup> more than justified the added procedural requirements and precautions mandated by its use.

Targets 30 through 34 were irradiated at power densities ranging from 0.955 to 1.362 MW/cm<sup>2</sup> and exhibited distinct, bright light emission indicative of plasma formation. Power densities were lowered to a range between 0.88 and 1.0 MW/cm<sup>2</sup> for irradiation of Targets 35 through 39. Light emission was again observed adjacent to each target surface although not as intense as in the case of Targets 30 through 34.

At this point in the experiment it appeared likely that the power density threshold for plasma formation in a vacuum would be lower than the threshold observed for targets irradiated in the atmosphere. Based on this assessment, the power density range was again lowered to a range between 0.633 and 0.846 MW/cm<sup>2</sup> for irradiation of Targets 40 through 44. Incident laser pulses on these target surfaces produced light emission of progressively decreasing intensity indicative of the formation of successively weaker plasmas as the threshold power density was approached.

A further reduced power density range between 0.427 and 0.528 MW/cm<sup>2</sup> was used for irradiation of Targets 45 through 49 in order to determine the approximate power density for onset of plasma formation. Target 46, which was irradiated with a power density of 0.427 MW/cm<sup>2</sup>, displayed no detectable light emission while irradiation of the other 4 targets in this series produced dim light emission indicative of weaker plasma formation.

After having successfully determined the approximate range of power densities wherein the plasma formation onset occurred, a final series of 5 targets was irradiated with power densities ranging from 0.434 to 0.460 MW/cm<sup>2</sup> in order to confirm the plasma formation power density threshold. Irradiation of these targets produced dim light emission of progressively weaker intensity consistent with the reduced power densities. Targets 52 and 54 were subjected to incident power densities of 0.442 and 0.434 MW/cm<sup>2</sup> respectively and exhibited very dim light emission indicative of very weak plasmas. The results of this experiment are summarized in Table 7.

On the basis of this experimental data and allowing for inaccuracies because of hot spots in the nonuniform laser beam and for procedural and equipment accuracy limitations, a plasma formation power density threshold range of 0.43 MW/cm<sup>2</sup>  $\pm$  12% was selected.

## **B. TARGET SURFACE DAMAGE**

### **1. Unipolar Arcing in the Atmosphere**

A thorough evaluation of the surface damage on all targets irradiated in the atmosphere yielded some very interesting results. Detailed examination of the target surfaces with both the scanning electron microscope and the optical microscope revealed that surface damage was confined solely to unipolar arcing on targets subjected to a single unfocused laser pulse.

The unipolar arcing damage mechanism was particularly evident on targets irradiated at power densities in excess of 1.5 MW/cm<sup>2</sup>. These targets exhibited well formed craters ranging in diameter from 5 to 8 microns with clearly distinguishable crater rims and darkened cathode spot areas 2 to 3 microns in diameter. Figure 4.1 illustrates a well formed unipolar arc crater representative of those observed on Targets 1-5. Unipolar arc crater densities varying from 150,000 to 800,000 craters/cm<sup>2</sup> were observed on these target surfaces. Figure 4.2 provides a photographic record of a typical crater density pattern indicative of target surfaces subjected to power densities in the 1.5-2.2 MW/cm<sup>2</sup> range.

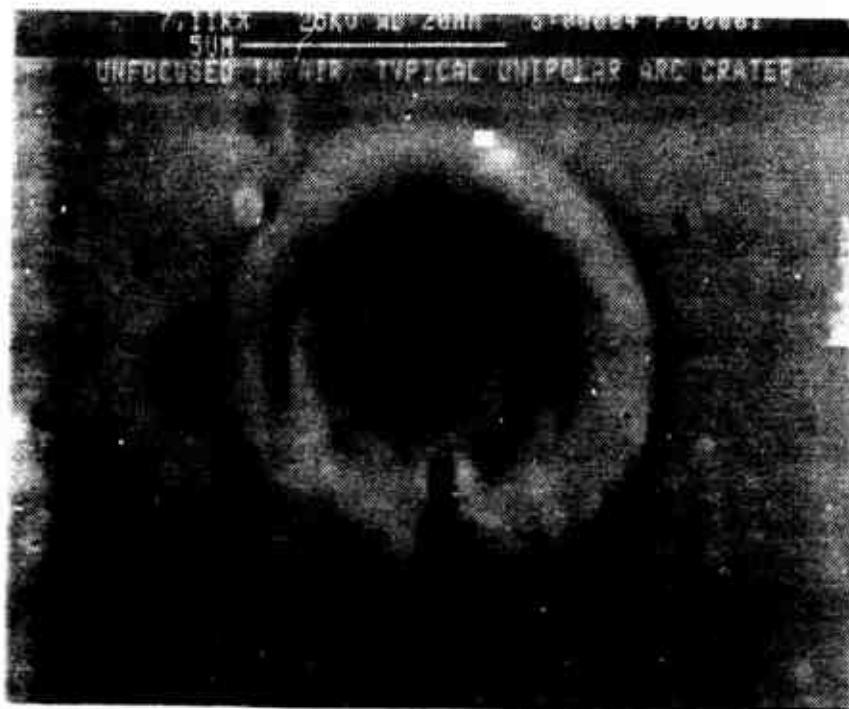


Figure 4.1 Unipolar Arc Crater on Polished SS 304  
Irradiated at Power Density of  $1.592 \text{ MW/cm}^2$ , SEM 7110X.

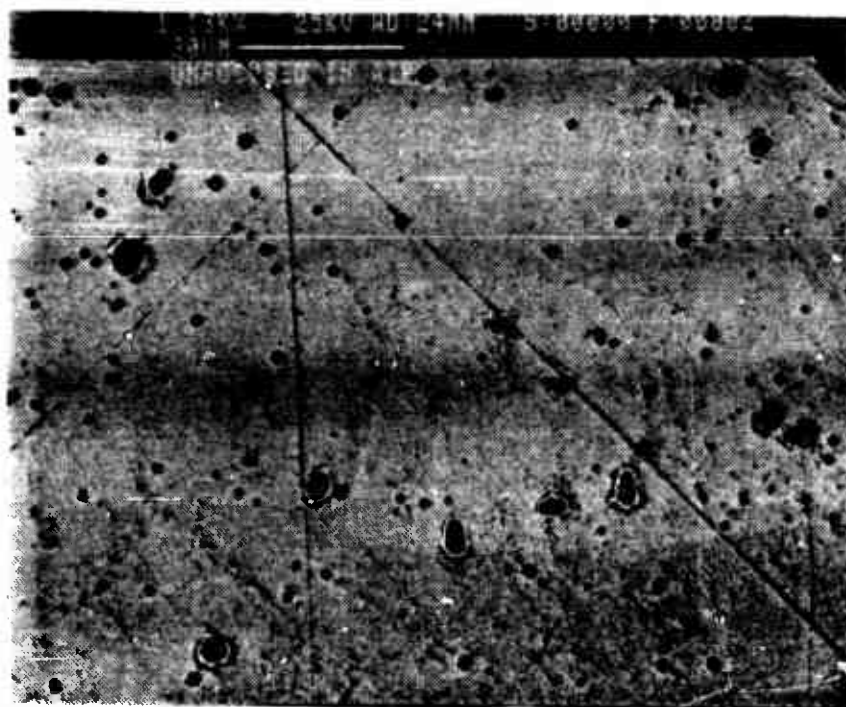


Figure 4.2 Unipolar Arc Crater Density Pattern on Polished SS 304  
Irradiated at Power Density of  $1.506 \text{ MW/cm}^2$ , SEM 1130X.

No surface damage features were noted on Targets 6 through 13. The absence of unipolar arcing on these target surfaces was consistent with previously described experimental findings which indicated no plasma formation. Initially it was thought that unipolar arc craters were being observed on these targets. Figure 4.3 is an example of a target surface area that was originally analyzed as containing unipolar arc craters. The faint halos surrounding darkened areas were incorrectly assumed to be unipolar arc craters and cathode spots respectively. However, upon further evaluation of this apparent damage with the topographical analyzer on the back scatter unit of the scanning electron microscope, it was found that there were no topographical differences between the faint halo and the darkened areas. These areas were evaluated as charging spots caused by the presence of micron size dust particles which were subjected to the electron beam in the scanning electron microscope. Subsequent to this finding, greater attention to detail with respect to target cleanliness was invoked while preparing targets for irradiation and evaluation. These measures resulted in enhanced target cleanliness and minimized the presence of charging spots as false indicators of unipolar arcing on subsequent targets.

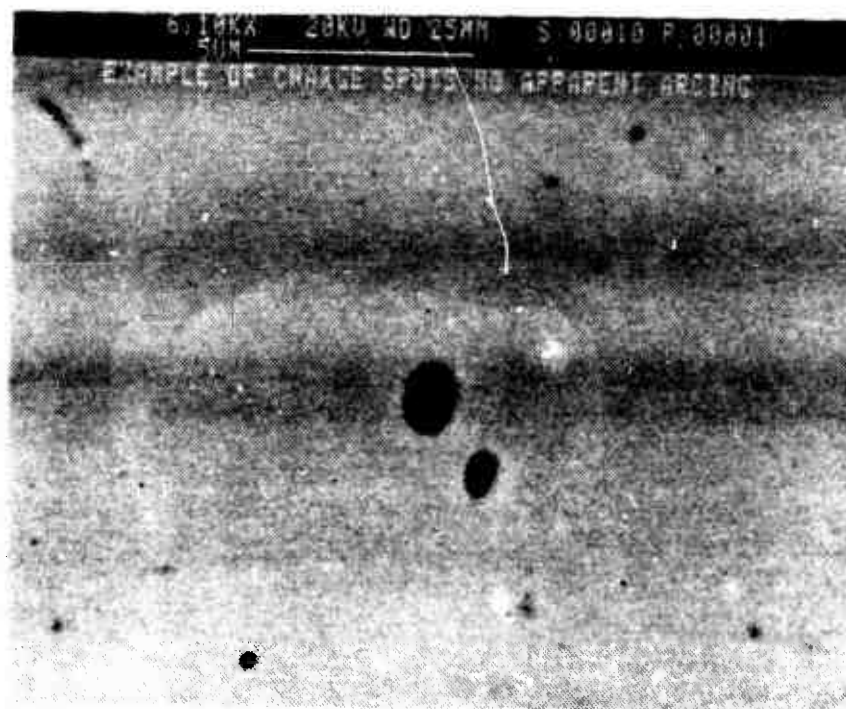


Figure 4.3 Charging Spots: False Indicators of Unipolar Arcing  
Observed on Target No. 10, SEM 6100X.

Although Targets 14 and 15 exhibited very dim light emission when irradiated, no evidence of unipolar arcing or any other damage could be found on either target surface. Apparently the weak plasmas adjacent to these target surfaces possessed electrons with insufficient energies to establish the floating potentials and electric fields necessary to ignite the arcing process.

Examination of Targets 16 and 17 revealed the presence of unipolar arcing damage over broad areas on both target surfaces. These targets were irradiated at 0.954 and 1.154 MW/cm<sup>2</sup> respectively. Figures 4.4 and 4.5 depict crater density patterns representative of those patterns observed over the entire surfaces of Targets 16 and 17 respectively. Comparison of Figures 4.4 and 4.5 revealed a significant decrease in crater density as power density was decreased and plasma formation threshold was approached. Crater densities ranging from approximately 500,000 to 750,000 cm<sup>-2</sup> were observed on Target 17. The surface of Target 16 was populated by significantly fewer craters and exhibited a crater density range of 150,000 to 200,000 cm<sup>-2</sup>. Figures 4.6 and 4.7 provide photographic evidence of crater features on Targets 16 and 17 respectively and are included to illustrate the differences in crater dimensions and rim characteristics associated with decreasing power density. The craters on Target 17 were well formed with diameters ranging from about 3 to 8 microns and displayed extensive rim structures. Craters on Target 16 were considerably smaller with diameters in the 1 to 3 micron range and displayed much less pronounced rim structure indicative of a less intense arcing process.

Targets 18 and 19 were designated as reference targets and were examined before and after irradiation with similar magnification on the scanning electron microscope. Both targets were purposely scratched in order to provide distinct geographical reference points for subsequent photographs.

Pictured in Figures 4.8 and 4.9 is the reference sector on Target 18 before and after irradiation. Except for a very few small dark areas, which appeared on Figure 4.8 and were believed to be material imperfections, the target surface exhibited features characteristic of a polished metallic finish. The reference sector containing unipolar arcing damage is displayed in Figure 4.9. The crater density on this irradiated surface was approximately 500,000 cm<sup>-2</sup>. Since Target 18 had been irradiated with a power density of 1.578 MW/cm<sup>2</sup>, the observed crater density was consistent with crater densities previously measured on Targets 1 through 5.

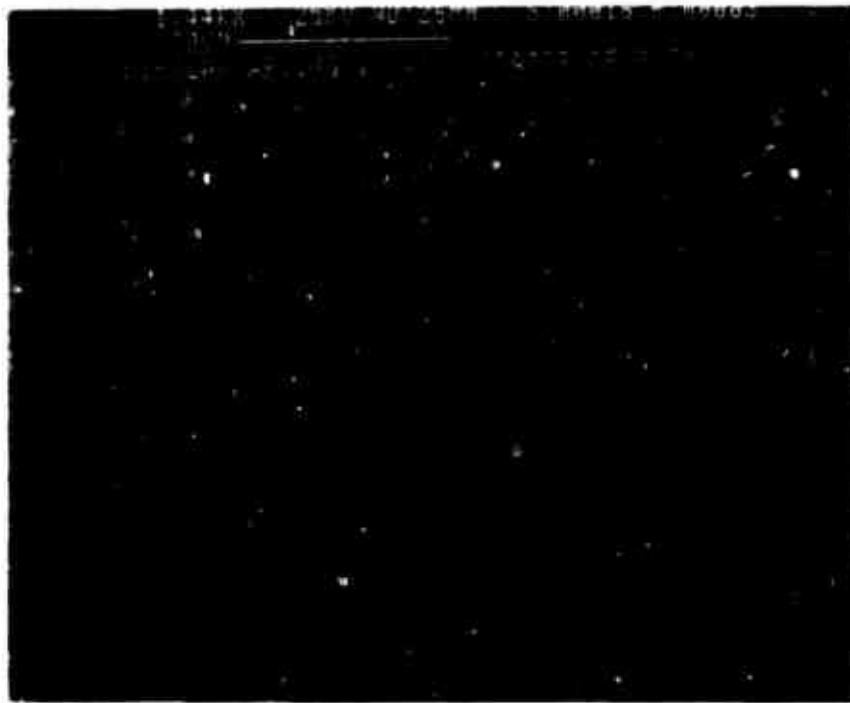


Figure 4.4 Unipolar Arc Crater Density Pattern on Polished SS 304  
Irradiated at Power Density of  $0.954 \text{ MW/cm}^2$ , SEM 1980X.

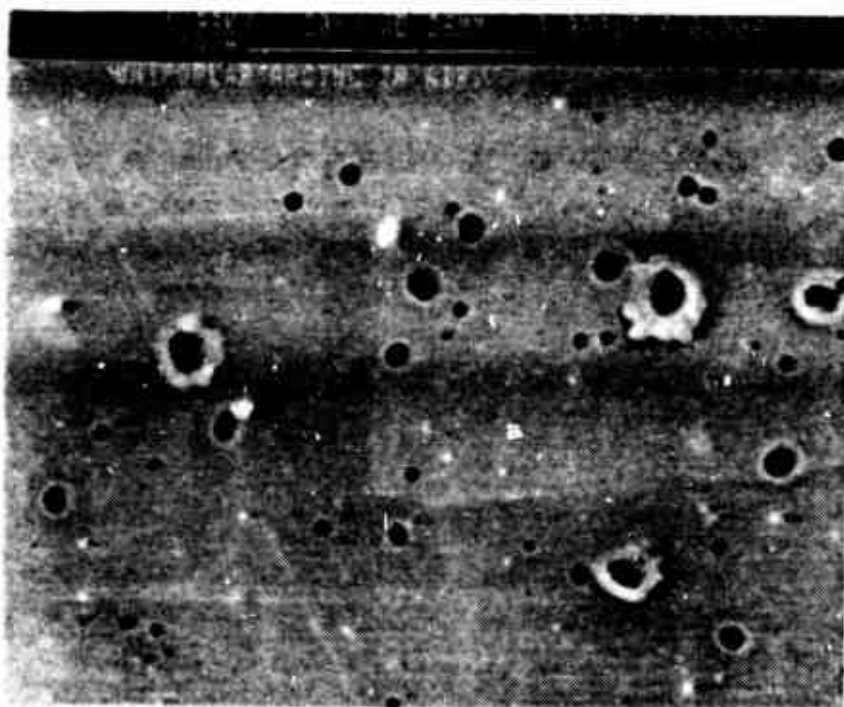


Figure 4.5 Unipolar Arc Crater Density Pattern on Polished SS 304  
Irradiated at Power Density of  $1.154 \text{ MW cm}^2$ , SEM 1440X.

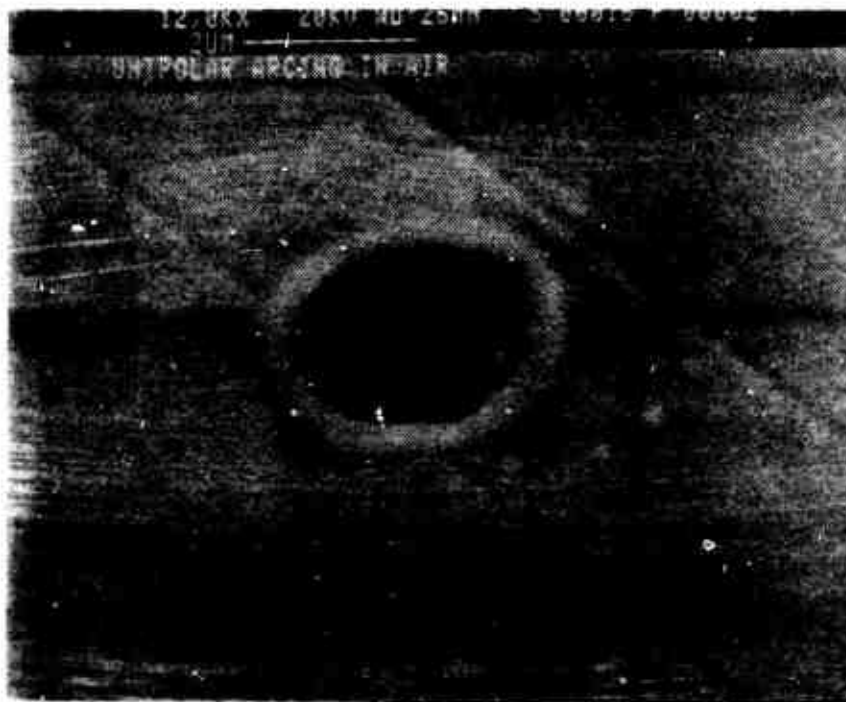


Figure 4.6 Small Unipolar Arc Craters on Polished SS 304 Irradiated at Power Density of  $0.954 \text{ MW/cm}^2$ , SEM 12000X.



Figure 4.7 Larger Well Developed Unipolar Arc Craters on Polished SS 304 Irradiated at Power Density of  $1.154 \text{ MW cm}^2$ , SEM 7920X.



Figure 4.8 Unradiated Polished SS 304 Reference Target No. 18, SEM 1420X.

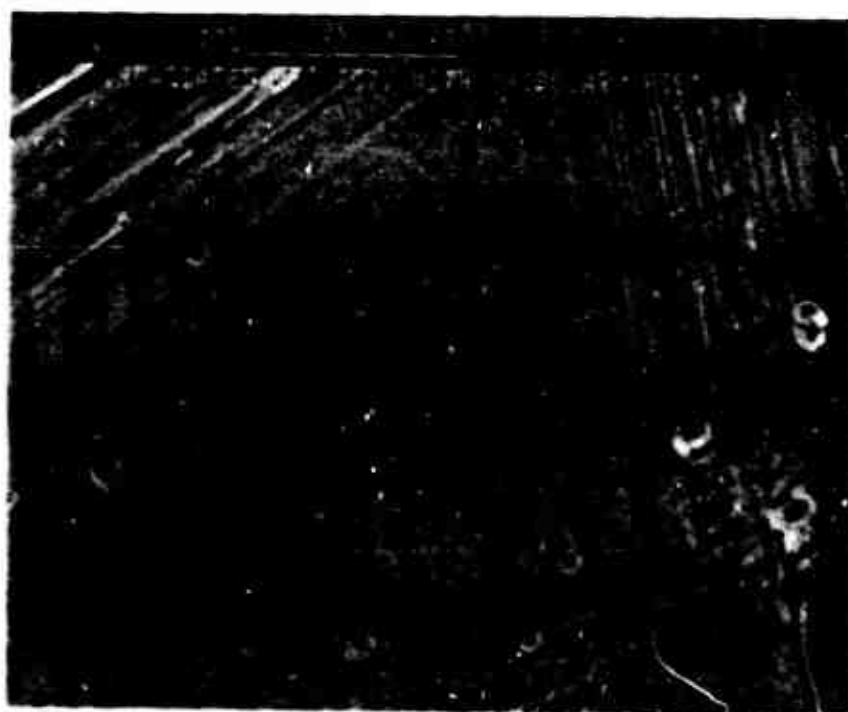


Figure 4.9 Crater Density Pattern on Reference Target No. 18  
Irradiated at Power Density of  $1.578 \text{ MW cm}^2$ , SEM 1440X.

Target 19 also served as a reference target but was irradiated with 6 laser pulses at a pulse repetition frequency of 0.5 Hz and an average power density of 1.421 MW cm<sup>2</sup>. The unirradiated sector is shown in Figure 4.10. The irradiated sector, displayed in Figure 4.11, illustrates the effects of a rapid sequential incidence of closely spaced laser pulses. It was particularly interesting to note that the damage on this target surface was not confined solely to unipolar arcing but consisted of a combination of unipolar arcing and thermal damage effects. A close examination of the target surface revealed unipolar arc craters which had been refilled with molten surface material that solidified after cessation of the pulse sequence. Additionally, river patterns indicative of a flowing molten surface material were in evidence on the target surface.

Targets 20 through 27 were irradiated in a power density range expected to contain the threshold value for plasma formation and resultant unipolar arcing damage. Although Targets 20 and 27 exhibited dim light emission indicative of weak plasma formation, neither target contained any evidence of surface damage. This was consistent with previously described findings for Targets 14 and 15 which indicated a plasma-surface interaction that was too weak to ignite the arcing process.

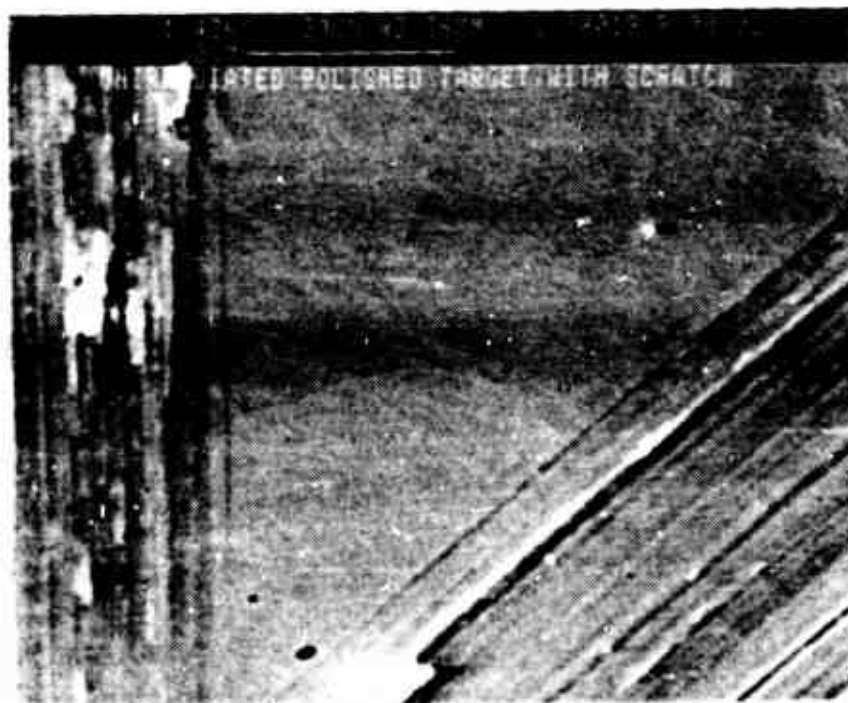
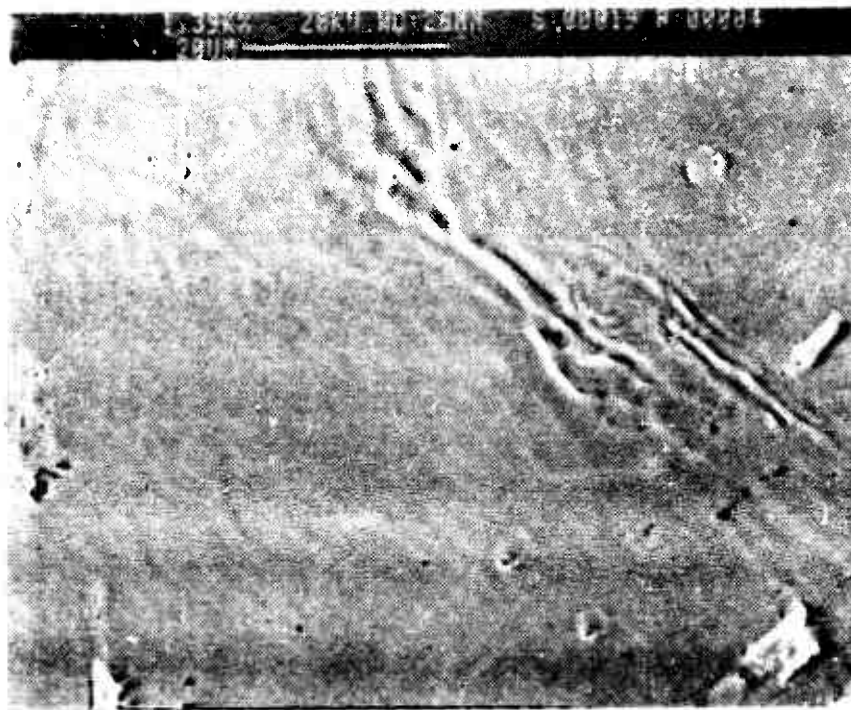


Figure 4.10 Unirradiated Polished SS 304 Reference Target No. 19. SEM 1420X.



**Figure 4.11 Surface Damage on Reference Target No. 19 Irradiated by a Series of 6 Pulses at PRF 0.5 Hz and Average Power Density of 1.421 MW/cm<sup>2</sup>, SEM 1390X.**

Illustrated in Figures 4.12 and 4.13 is the limited surface damage found on Targets 23 and 25 respectively. As the power density was reduced and approached the plasma formation threshold, crater density continued to decrease as expected.

A detailed examination of Target 26 revealed a sparsely distributed array of very small unipolar arc craters with barely discernible rim characteristics. Since the unipolar arcs were not well developed, confirmation of their existence required the use of the topographical analyzer of the scanning electron microscope. Figure 4.14, which provides a split screen view of the scanning electron microscope image and the topographical analyzer picture, clearly confirmed topographical differences indicative of arc craters. The very limited damage observed on this target was consistent with previously described experimental results which indicated the formation of a weak plasma containing electrons with energy just sufficient to establish the floating potential and electric field necessary to initiate the arcing mechanism.

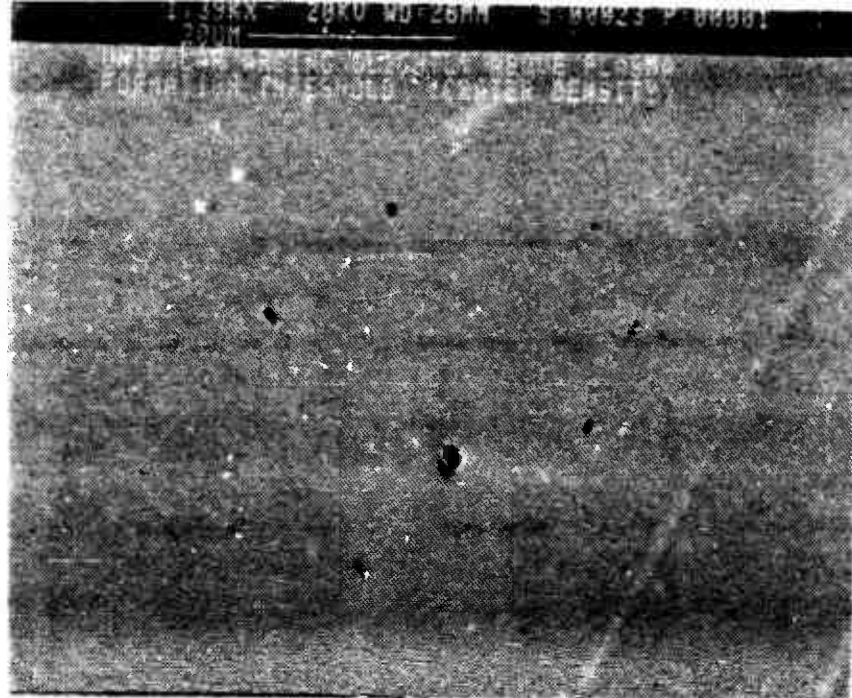


Figure 4.12 Unipolar Arc Crater Density Pattern on Polished SS 304  
Irradiated at Power Density of  $0.918 \text{ MW/cm}^2$ , SEM 1390X.

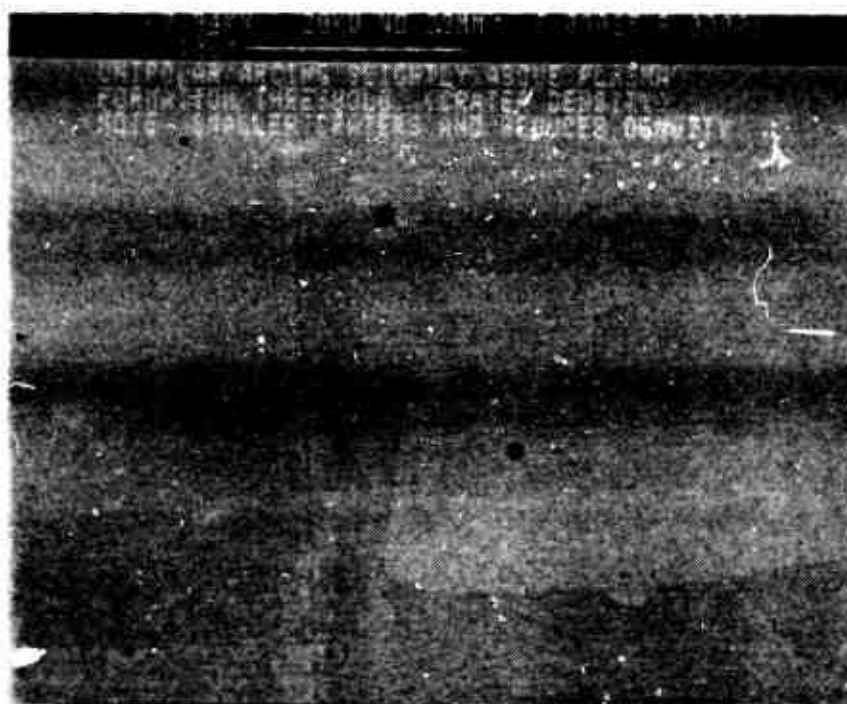


Figure 4.13 Unipolar Arc Crater Density Pattern on Polished SS 304  
Irradiated at Power Density of  $0.885 \text{ MW cm}^2$ , SEM 2940X.

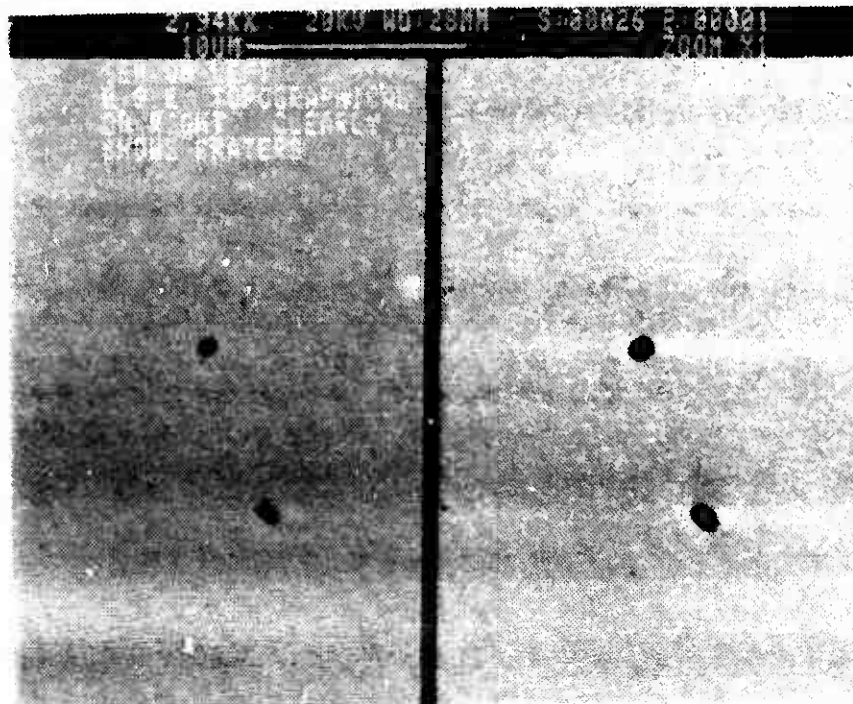


Figure 4.14 Sparsely Distributed Small Unipolar Arc Craters on Polished SS 304  
Irradiated at Power Density of  $0.884 \text{ MW/cm}^2$ , Very Slightly  
Above the Plasma Formation Threshold, SEM 2940X.

## 2. Unipolar Arcing in a Vacuum

A thorough examination of the damage resident on each target surface was accomplished using the scanning electron microscope. Damage characteristics somewhat different than those found on targets irradiated in the atmosphere were observed. Apparent enhancement of thermal coupling on targets irradiated in the vacuum at power densities between  $0.955$  and  $1.362 \text{ MW/cm}^2$  produced damage features which were predominantly unipolar arcing related but also included limited thermal damage effects. On targets irradiated near the power density threshold for plasma formation, only unipolar arcing damage was evident, as expected.

Examination of Targets 28 and 29 revealed the absence of unipolar arcing damage. This experimental finding was consistent with previous results which indicated no plasma formation on these target surfaces.

Targets 30 through 36, which were subjected to power densities moderately above the plasma formation threshold in a range from 0.955 to 1.362 MW/cm<sup>2</sup>, displayed a combination of unipolar arcing and limited thermal damage effects. Figure 4.15 displays a relatively large unipolar arc crater typical of those observed on these target surfaces. Particularly noteworthy was the area extending radially approximately 10 to 12 microns from the crater rim. This area appeared to contain resolidified surface material that was melted during an intense arcing process and was distributed radially over the area adjacent to the crater. Smaller craters present on the damaged surface appeared to be partially backfilled with resolidified surface material.

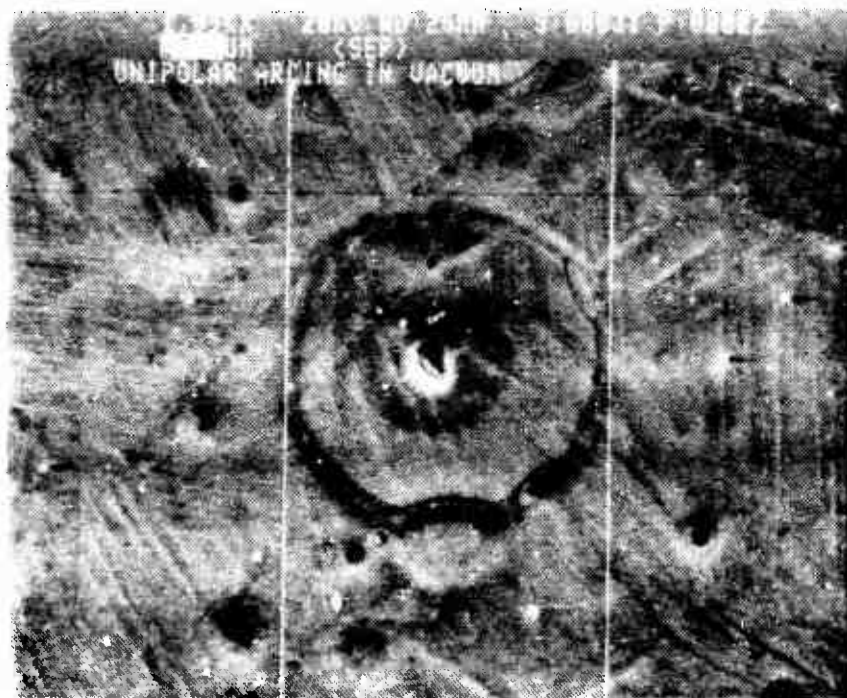


Figure 4.15 Unipolar Arc Crater on Polished SS 304  
Irradiated at Power Density of 1.193 MW/cm<sup>2</sup>, SEM 1890X.

As typified by Figure 4.16, moderately high crater densities ranging from 600,000 to 950,000 cm<sup>-2</sup> were exhibited on these damaged surfaces. As can be readily seen by examination of Figure 4.16, the unipolar arc craters contained distinct cathode spots consistent with the Unipolar Arcing Model previously described in the background and theory chapter of this study. Generation of comparable crater density patterns observed on targets irradiated in atmosphere required higher power densities in the 1.5 to 2.2 MW/cm<sup>2</sup> range. This finding was yet another indication of the enhanced plasma-surface coupling which occurred in the vacuum.

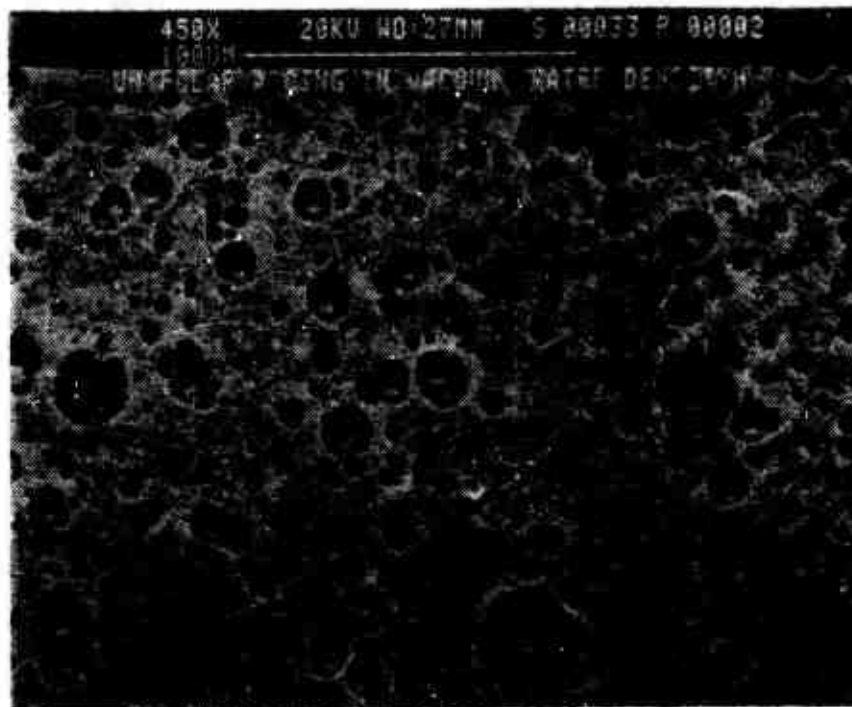


Figure 4.16 Unipolar Arc Crater Density on Polished SS 304  
Irradiated at Power Density of  $1.362 \text{ MW/cm}^2$ , SEM 450X.



Figure 4.17 Unipolar Arc Crater Density Pattern on Polished SS 304  
Irradiated at Power Density of  $0.764 \text{ MW/cm}^2$ , SEM 1400X.

A thorough study of the surface damage features on Targets 37 through 44 revealed the presence of unipolar arc craters which decreased in size and density as incident laser pulse energy density was progressively decreased. Illustrated in Figure 4.17 is a unipolar arc crater density pattern representative of those density patterns observed on these targets. Unipolar arc densities ranging from approximately 300,000 to 600,000  $\text{cm}^{-2}$  were noted.

Figures 4.18 and 4.19 are provided to illustrate the typical unipolar arc crater dimensions found on target surfaces irradiated in the power density range utilized for the vacuum experiment. Pictured in Figures 4.18 and 4.19 are unipolar arc craters with diameters of approximately 7.6 and 5.1 microns for targets irradiated with power densities of 1.008 and 0.633  $\text{MW}/\text{cm}^2$  respectively.

Examination of Targets 45 through 49, which were irradiated with power densities very close to the plasma formation threshold, revealed significant reductions in the size and extent of surface damage. Depicted in Figures 4.20 and 4.21 is a small unipolar arc crater which was produced at a power density of 0.480  $\text{MW}/\text{cm}^2$  on Target 45. This symmetric crater exhibited a distinct cathode spot 0.45 microns in diameter and a rim to rim diameter of approximately 1.75 microns. Although the rim structure was well formed and clearly visible, its relatively small size indicated a very short arcing duration which was consistent with the formation of a weak plasma generated by the low incident laser pulse power density. Craters of comparable size and structure were sparsely distributed over the surfaces of these targets.

Shown in Figure 4.22 is the unipolar arc density pattern observed on the surface of Target 47. This target was irradiated with a power density slightly above the plasma formation threshold and exhibited a unipolar arc crater density less than 150,000  $\text{cm}^{-2}$ .

Detailed study of Targets 50 through 54, which were irradiated with power densities very close to the plasma formation threshold, revealed further reductions in the extent of surface damage. Pictured in Figures 4.23 and 4.24 are small diameter unipolar arc craters typical of those craters observed on Target 50 and 52. These craters were similar in structure to those observed on Targets 47 and 48 but were slightly smaller in dimensions and much more sparsely distributed. After a very careful search of each target for evidence of damage, fewer than 100 unipolar arc craters were identified on either surface.



Figure 4.18 Unipolar Arc Crater on Polished SS 304  
Irradiated at Power Density  $1.008 \text{ MW/cm}^2$ , SEM 5890X.



Figure 4.19 Unipolar Arc Crater on Polished SS 304  
Irradiated at Power Density  $0.633 \text{ MW/cm}^2$ , SEM 12,000X.

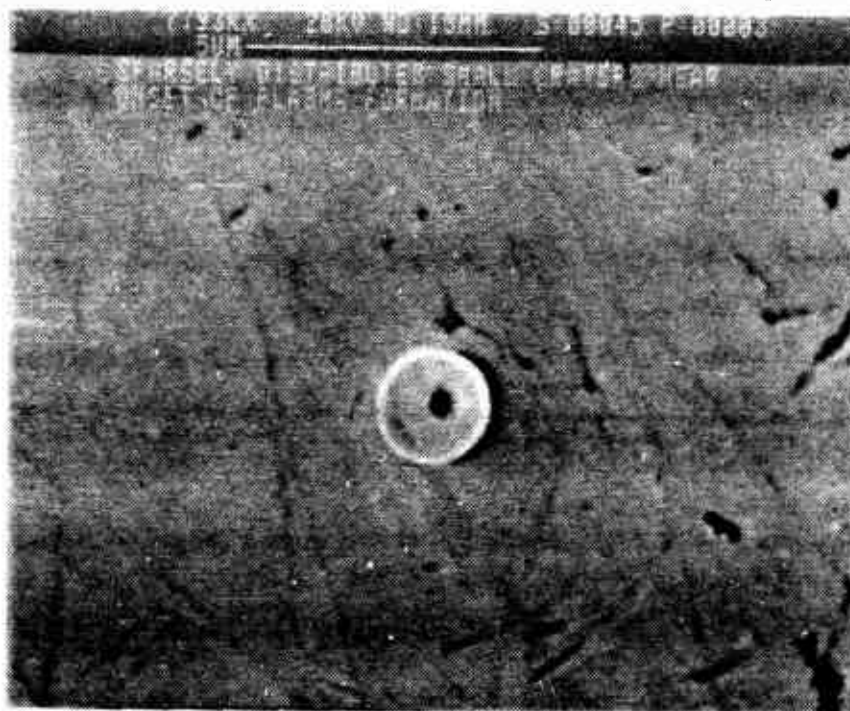


Figure 4.20 Small Unipolar Arc Crater on Polished SS 304 Irradiated at Power Density of  $0.480 \text{ MW/cm}^2$ , SEM 7930X.

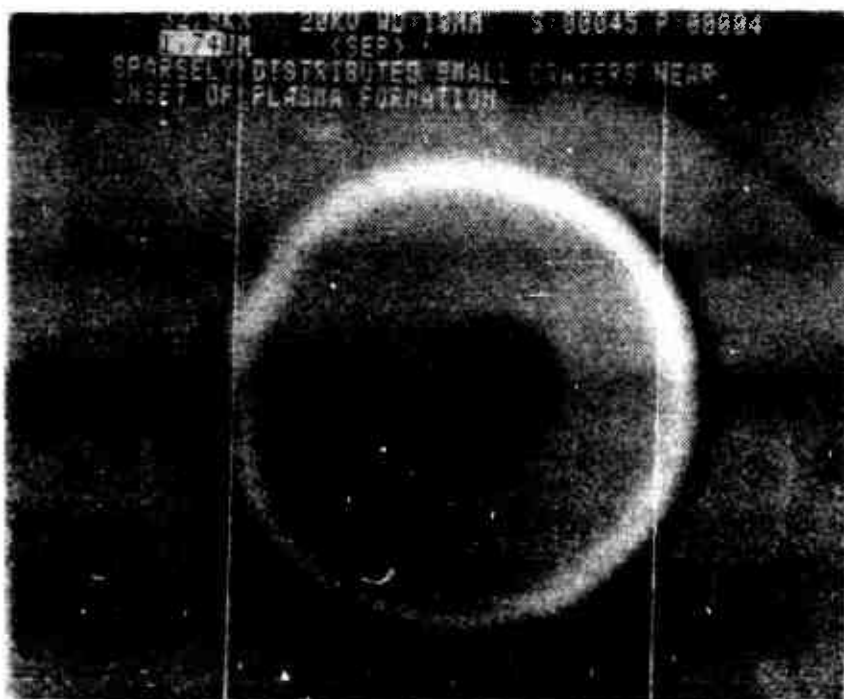


Figure 4.21 Small Unipolar Arc Crater on Polished SS 304 Irradiated at Power Density of  $0.480 \text{ MW/cm}^2$ , SEM 32,800X.

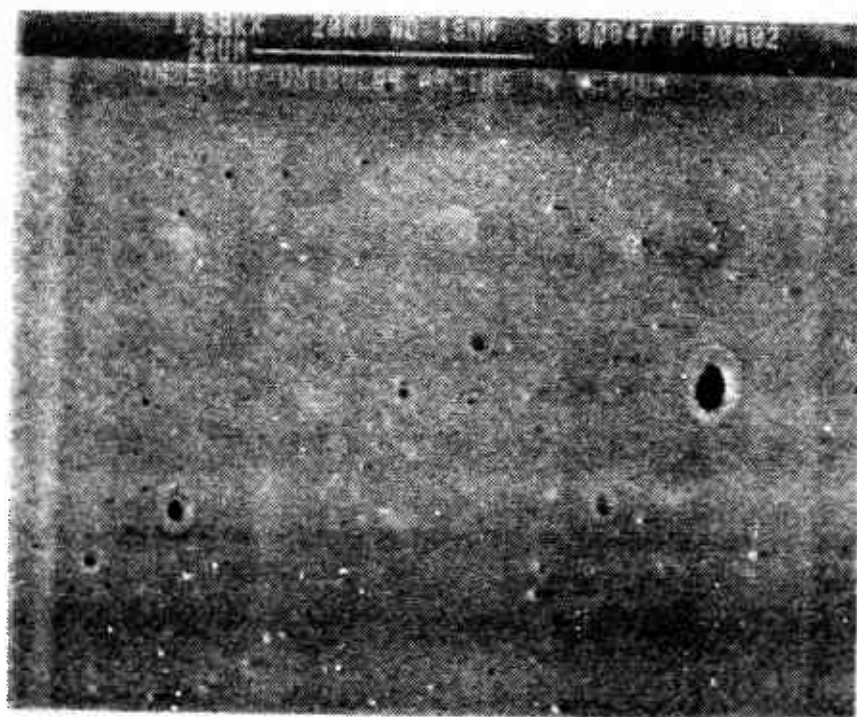


Figure 4.22 Unipolar Arc Crater Density Pattern on Polished SS 304 Irradiated at Power Density of  $0.467 \text{ MW/cm}^2$ , SEM 1880X.

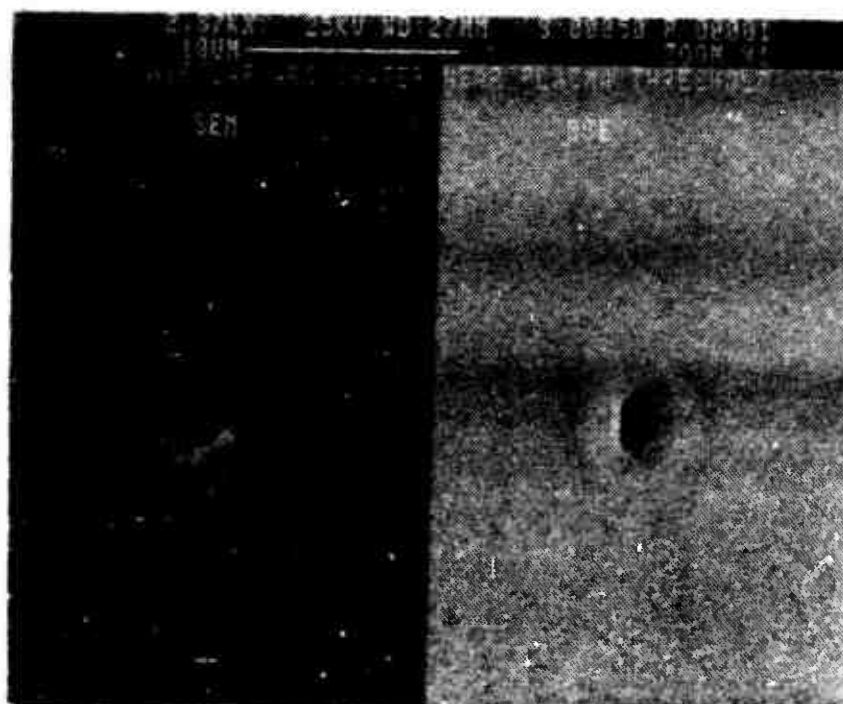


Figure 4.23 Unipolar Arc Crater on Polished SS 304 Irradiated at Power Density of  $0.460 \text{ MW/cm}^2$ , SEM 2870X View on Left, Topographical Confirmation on Right.

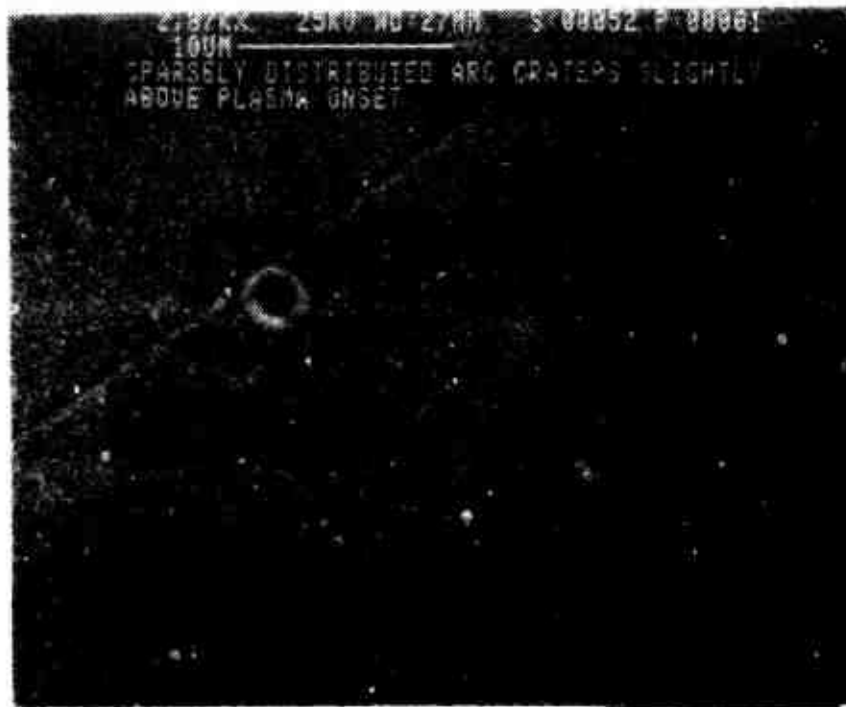


Figure 4.24 Unipolar Arc Craters on Polished SS 304 Irradiated at Power Density of  $0.450 \text{ MW/cm}^2$ , SEM 2870X.

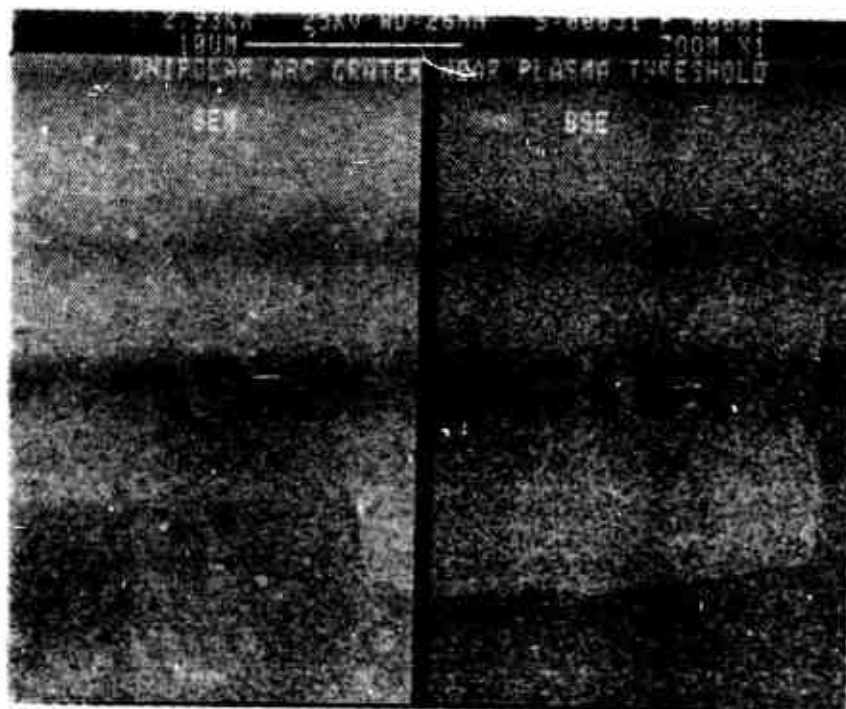


Figure 4.25 Unipolar Arc Crater on Polished SS 304 Irradiated at Power Density of  $0.442 \text{ MW/cm}^2$ , Nearly Coincident with the Plasma Formation Threshold, SEM 2930X.

Displayed in Figure 4.25 is a very weakly formed crater indicative of the extremely low level of damage observed on Target 51. This target was irradiated with a power density very nearly coincident with the plasma formation threshold and exhibited very dim light emission indicative of weak plasma formation. After a painstaking careful two hour search of the target surface, only six unipolar arc craters were identified and confirmed using the scanning electron microscope with very high resolution and the topographical analyzer of the electron back scatter unit.

## C. DISCUSSION OF RESULTS

### 1. Introduction

A comprehensive evaluation of the experimental results presented in this chapter, including quantitative comparison with the results of a previous similar experiment as well as a comparison of the results obtained in the atmosphere and in a vacuum, was undertaken to add completeness and continuity to this study.

### 2. Quantitative Comparison with Previous Results

Before comparing the experimental results of the vacuum experiment with those of a similar experiment conducted by Beelby and Ulrich in 1981 [Ref. 8], a review of the differences in the experiments was necessary. Beelby and Ulrich utilized a Korad 1500 neodymium glass laser of nominal wavelength 1.06 microns, a laser pulse duration of 20 nanoseconds, and a focused beam to irradiate SS 304 stainless steel targets in a  $10^{-6}$  torr vacuum. The vacuum experiment reported herein was conducted using a Lumonics CO<sub>2</sub> TEA high energy pulsed laser with a wavelength of 10.6 microns, a pulse duration of 4.55  $\mu$ sec., and an unfocused beam. It was significant to note that the nominal values for the wavelength and pulse width used in this experiment exceeded those used by Beelby and Ulrich by factors of 10 and 227.5 respectively.

Whereas the study reported herein examined 27 SS 304 targets irradiated in a fairly narrow range of power densities near the plasma formation threshold, Beelby and Ulrich examined a comparatively small number of 10 SS 304 targets irradiated with power densities in a relatively wide range between 5.1 and 64.4 MW/cm<sup>2</sup>.

Beelby and Ulrich estimated that the plasma formation power density threshold for SS 304 irradiated in a vacuum was approximately 5.4 MW/cm<sup>2</sup> and indicated that their results were of order of magnitude quality only because of a variety of experimental limitations. The plasma formation power density threshold for the vacuum experiment reported herein was  $0.43 \text{ MW/cm}^2 \pm 12\%$ . Differences in these

plasma formation power density thresholds are believed to be attributed to the significant differences in laser wavelengths, pulse durations and the resultant laser-surface coupling associated with the experiments.

Although the power density thresholds in these experiments differed by approximately one order of magnitude, there were some striking similarities between the experiments, particularly with respect to observed target surface damage. Experimental results in both studies proved conclusively that unipolar arcing constituted the dominant laser damage mechanism at power densities near the plasma formation threshold, and that the presence of a plasma was a necessary prerequisite for initiation of unipolar arcing. Additionally, the dimensional features displayed by the unipolar arc craters produced at power densities near plasma onset in both studies were typically 1-2 microns in diameter with distinct, symmetric rim structure.

### 3. Comparison of Atmospheric and Vacuum Experiment Results

The power density thresholds for plasma formation in the atmosphere and in the vacuum were determined to be  $0.88 \text{ MW/cm}^2 \pm 12\%$  and  $0.43 \text{ MW/cm}^2 \pm 12\%$  respectively. A reasonable explanation for the difference in these results must necessarily include an assessment of laser pulse cutoff and the conditions which caused its occurrence.

As previously described in the background and theory chapter of this thesis, plasma cutoff for the 10.6 micron wavelength produced by the  $\text{CO}_2$  laser occurred at a critical density of  $9.93 \times 10^{18}/\text{cm}^3$ . The standard atmosphere, unlike the  $10^{-6}$  torr vacuum, possessed a comparatively large inventory of neutral atoms, with a number density of approximately  $3 \times 10^{19}/\text{cm}^3$ , which established initial conditions for a much more rapid ionization process than in the case of the vacuum. Because of the reduced period required to reach the critical density and plasma cutoff, the amount of time available for the incident laser pulse to interact with the target surface was limited. The atmosphere adjacent to the target surface apparently influenced the electron heating by slowing down the energy absorption process. The higher power density required for plasma formation in the atmosphere was confirmed by experimentation.

It should also be noted that, because of the relatively large spot size and resultant low power densities used in these experiments, laser pulse breakdown in air was not encountered.

#### 4. Comparison of Unfocused and Focused Pulse Experimental Results

The results of a comparable vacuum experiment, conducted by Weston and reported in [Ref. 13], revealed that the power density threshold required for plasma formation on a SS 304 target, which was irradiated in a  $10^{-6}$  torr vacuum with a focused pulse of approximately  $1 \text{ cm}^2$ , was approximately  $0.41 \text{ MW/cm}^2$ . This threshold for plasma formation was consistent with the experimental findings reported herein.

## V. CONCLUSIONS AND RECOMMENDATIONS

The primary purpose of this thesis was to determine the laser pulse power density threshold required to produce a plasma on SS 304 stainless steel targets and to thoroughly investigate the laser damage mechanism. The primary objective was accomplished by means of a detailed examination of the plasma-surface effects on these target surfaces. Targets were irradiated using an unfocused beam with a spot size of approximately  $2 \text{ cm}^2$  during two experiments which were conducted at atmospheric pressure and in a  $10^{-6}$  torr vacuum.

The secondary purpose of this thesis was to clearly demonstrate the value of the  $\text{CO}_2$  laser as a viable research instrument in the study of the laser damage mechanism and to thoroughly document details of its use in order to encourage and facilitate additional research. This purpose was achieved by the successful conduct of the two previously described experiments.  $\text{CO}_2$  laser operations were thoroughly documented in this report which included a chapter on experimental design and a description of the laser system and ancillary equipment, an appendix containing the laser operating procedure and safety requirements, and a laser pulse energy repeatability study.

### A. QUALITATIVE COMPARISON OF EXPERIMENTAL RESULTS WITH THE THEORETICAL MODEL

The background and theory chapter of this thesis identified ion sputtering, thermal evaporation and unipolar arcing as potential contributors to the laser damage mechanism. Although ion sputtering and thermal evaporation were certainly instrumental in initial plasma formation, they did not constitute a major damage mechanism. Unipolar arcing, however, was determined to be the primary laser damage mechanism observed on SS 304 targets irradiated with an unfocused beam in atmosphere and in a vacuum. In the vacuum experiment at power densities moderately above the plasma formation threshold, a small degree of surface melting, indicative of very limited thermal effects, was noted. At power densities near the plasma formation threshold in both experiments, target surface damage was confined solely to unipolar arcing. These results were completely consistent with the theoretical expectations of the Sequential Unipolar Arcing Model.

## B. PLASMA FORMATION POWER DENSITY THRESHOLD

Power density thresholds for the atmospheric pressure and for the  $10^{-6}$  torr vacuum experiments were determined to be  $0.88 \text{ MW/cm}^2 \pm 12\%$  and  $0.43 \text{ MW/cm}^2 \pm 12\%$  respectively. The higher power density required for plasma formation in atmosphere was attributed to the retarding influence of the atmosphere adjacent to the target surface on the energy absorption process. Rapid ionization of the neutral atoms, resident in the atmosphere near the target surface, resulted in an earlier plasma cutoff of the incoming laser pulse and reduced the time available for plasma-surface interaction. Therefore, a laser pulse with higher power density was required to produce a plasma in atmosphere.

## C. RECOMMENDATIONS

Of the various experimental limitations encountered during this research, the most significant was nonuniformity of energy distribution in the laser pulse. Since this limitation contributed the largest experimental error factor, measures should be taken to reduce or eliminate it before future experiments are conducted with the  $\text{CO}_2$  pulsed laser. The procurement and use of an unstable resonator with the  $\text{CO}_2$  laser facility would certainly reduce the uncertainty of experimental results which depend on laser pulse energy content and distribution.

It is strongly recommended that the dependence of plasma-surface effects on pulse duration be further investigated in future research work. In order to facilitate this in depth research, more durable optics, including beam splitters and vacuum chamber windows with the ability to withstand higher energy fluxes, need to be obtained.

Serious thought should be given to constructing a clean room around the  $\text{CO}_2$  laser facility. By controlling temperature, humidity, dust particulate in the atmosphere and vacuum chamber pump exhaust, a more favorable experimental environment would be created in which better consistency of results could be reasonably expected.

## APPENDIX A

### LUMONICS TE-822 HP CO<sub>2</sub> LASER OPERATING PROCEDURE

Although the CO<sub>2</sub> high energy pulsed laser is an excellent research instrument for the study of plasma surface interactions, it must be operated in strict accordance with applicable safety precautions and operating procedures in order to continually ensure the safety of operators and the protection of equipment.

Prior to operating the laser system, an individual must complete a retina scan eye examination to comply with OSHA requirements. Prospective operators must become thoroughly familiar with all procedural and safety aspects of the laser system and receive a systems operation orientation from the Physics Department Plasma Lab Technician and demonstrate the ability to safely operate the system prior to being designated in writing as a laser facility supervisor. It should be noted that at least two individuals, one of whom is a qualified laser facility supervisor, must be present in the plasma laboratory at all times when the laser system is in operation.

Complete awareness of the potential hazards associated with the laser system operation is a necessary prerequisite for prospective laser facility supervisors. One of these hazards arises because the 10.6 micron wavelength of CO<sub>2</sub> is outside of the visible spectrum, and therefore, inadvertent exposure of the eyes and other body parts to the high energy laser beam is a definite possibility if necessary precautions are not routinely enforced. These precautions include the wearing of protective safety glasses by all personnel present in the plasma laboratory during laser system operation and the verification that all openings to the plexiglass experiment area enclosure are shut before firing the laser. The high voltage, resident in the power supplies inside the laser cabinet, presents a potential electrical hazard if safety precautions are not properly heeded. All operators must ensure that the laser cabinet covers are securely in place prior to operating the laser and that any troubleshooting of the electrical system is accomplished only by a qualified technician who completely understands

high voltage power supplies and the hazards associated with capacitor discharge. Since the energy content of the laser beam can be quite large, the possibility of a laser induced fire can not be overlooked. This is particularly important when making spot size recordings on paper because the incidence of a series of rapid pulses on the paper will likely ignite it. Therefore, when measuring spot sizes, use single shots spaced at prudent intervals to avoid fires.

The laser is equipped with a variety of system interlocks designed to prevent the operation of the system under conditions which would ultimately lead to personal injury or cause equipment damage. UNDER NO CIRCUMSTANCES will these interlocks be overridden or modified in any manner without the prior notification and consent of the Plasma Lab Technician and the written approval of the appropriate department chairmen with cognizance over the laser facility. These electrical interlocks, which are contained in the laser pulse initiation circuit, include:

A. Laser Enclosure Cover Interlocks (2) - ensure that electrical shock from the high voltage power supplies and interior electrical components is avoided during laser operation.

B. Laser Output Port Protective Cover Removed - ensures that the laser is not inadvertently pulsed with the output port protective cover in place causing reflection back into the internal optics and a high probability of damage.

C. Cooling Water Flow - ensures that proper cooling water flow and pressure are maintained in the laser system so that the temperature sensitive high voltage power supplies do not overheat and fail on thermal overload. Thermal interlocks associated with the high voltage power supplies are designed to trip on temperatures in excess of 125° F.

D. Laser Power Key - ensures that power is not available to the laser system until consciously applied by the operator.

E. Gas ON/OFF Switch - ensures that high voltage is not applied to the firing circuit unless gas flow has been properly established in the laser.

F. Plasma Laboratory Door - ensures that the laser system firing circuit will be temporarily disabled if the laboratory door is opened during laser system operation. The door audible alarm alerts operators of this problem.

Thus, although it can be seen that the interlock system does afford considerable safety, electrical interlocks can never replace the requirement for an alert and conscientious operator. It is with this in mind that the following operational procedure is provided. The basis for the procedural sequence is contained within the Lumonics TE-822 HP Instruction Manual [Ref. 25].

Laser System Start-Up is accomplished by following these sequential procedural steps:

1. Initiate cooling water flow and set the thermostat on the chill water unit to 15 °C.

2. Activate the Laboratory Door Interlock by placing the toggle switch on the control box to the left of the door to the ON position.

3. Set the MODE SELECT switch to SINGLE and the MULTIPLIER setting to X10.

#### NOTE

The MULTIPLIER control setting has three positions which are X.1, X1, and X10. These settings are used in conjunction with the INTERNAL RATE potentiometer and apply their stated multiplication factors to establish a desired pulse repetition frequency. In the X1 and X10 positions the capacitors in the laser firing circuit are continuously charged, and the front panel voltmeter continuously registers the high voltage power supply voltage level. In SINGLE shot mode, repetitive pulsing is not possible but the X10 MULTIPLIER setting is used so that the high voltage power supply voltage can be monitored continuously during the conduct of the laser start up procedure.

4. Open the Helium, Carbon Dioxide and Nitrogen cylinder valves and adjust each pressure regulator to 10 psig.

5. Turn the LASER POWER KEY to ON and note that the GAS OFF indicator is GREEN, the INTERLOCKS OPEN indicator is WHITE and the WARM UP INCOMPLETE indicator is YELLOW.

6. Slowly open the HEAD EXHAUST VALVE by placing the valve operator, which is located in the lower right hand corner of the front control panel, in the vertical position.

#### CAUTION

Failure to open the HEAD EXHAUST VALVE will cause the Head to quickly become overpressurized. It is equipped with a NON-RESETTABLE 5 psig pressure relief valve. Opening of this relief valve will place the laser system out of commission until a replacement valve is installed.

7. Depress the GAS ON pushbutton and observe that the RED GAS ON indicator is lit while the GREEN GAS OFF indicator is extinguished.

8. After gas flow is initiated, verify that the three gas bottle regulators are set at 10 psig. Adjust the settings as necessary.

## CAUTION

Consult the Laser Instruction Manual and ensure that only gases of the specified purity characteristics are utilized in the laser system.

9. Adjust the 6 Brooks flowmeters (three on the front control panel and three on the rear panel) to the desired flowrates recommended in the Laser Instruction Manual. Standard long pulse gas settings which are recommended for high voltage power supply settings up to 33 kV and pulse repetition frequencies  $\leq 10$  Hz are 8 SCFH for  $N_2$  and  $CO_2$  and 6 SCFH for He.

10. The INTERLOCKS OPEN indicator should be lit as the warm up proceeds.

11. Allow the gas purge to continue for a minimum of 15 MINUTES if the laser has been shut down for a lengthy period. During periods of frequent operation, a 5 MINUTE purge is adequate to flush the system and is strongly recommended in the interest of conserving gases.

12. Open the air cylinder and set the pressure regulator in the 16-24 psig range and establish a flowrate of 4 SCFH by adjusting the 6 flowmeters on the rear panel.

13. After the WARM UP INCOMPLETE indicator is extinguished (approximately one minute after the application of AC power) and the gas purge has been completed, the INTERLOCKS OPEN indicator will remain lit until the protective cover on the laser output port is removed at which time the INTERLOCKS OPEN indicator will be extinguished.

14. Set the HV CONTROL knob fully counterclockwise to its MINIMUM setting and depress the RED HIGH VOLTAGE ON pushbutton.

15. Turn The HV CONTROL knob clockwise until the voltmeter indicates 26 kV.

## CAUTION

Before commencing to pulse the laser VERIFY that the plexiglass experiment area enclosure is completely closed, that a laser beam absorbing stopper is positioned in the beam path at least one meter away from the output port and that all personnel in the plasma laboratory are wearing protective safety glasses. NEVER allow the high voltage to exceed 40 kV because this will inevitably result in the premature failure of the High Voltage Power Supplies.

16. The laser should now fire each time the SINGLE fire pushbutton is depressed.

17. In the event the laser DOES NOT FIRE, adjust the spark gap air pressure down in small increments until the laser pulses consistently.

18. Turn off the high voltage by depressing the HIGH VOLTAGE OFF pushbutton.

19. Position the MULTIPLIER switch to X.1, the INTERNAL RATE to 5 Hz and the MODE SELECT switch to MULTIPLIER.

20. Depress the HIGH VOLTAGE ON pushbutton and observe the laser pulsing at 0.5 Hz.

The laser is now fully prepared to support experimentation, but before doing so it is recommended that recording paper be used to determine the laser burn pattern. Comparison of this burn pattern with the nominal 30 mm by 33 mm pattern will provide a good indication that the laser is properly aligned and operating satisfactorily.

When the laser system has been secured for a relatively short period of several hours and the gas mix has been preserved in the head, the 15 minute gas purge is not required and a modified START-UP procedure may be employed which consists of the following sequential steps:

1. Turn on AC power.
2. Initiate and verify correct cooling water temperature and flowrate.
3. Open the HEAD EXHAUST VALVE and initiate and adjust gas pressures and flowrates.
4. After completion of warm-up and satisfying conditions to close all interlocks, initiate high voltage. When the GREEN HIGH VOLTAGE OFF indicator lights up, the laser is prepared to operate.
5. Subsequent to the completion of the laser system start up requirements and verification that ALL safety precautions have been met, the laser system may be safely operated.

The graphical depiction of laser pulse energy in joules versus laser high voltage power supply voltage level, contained in Figure A.1, was provided to assist future laser operators in the selection of appropriate experimental parameters. The long pulse gas mixture settings, previously described in this thesis, were used to establish the initial conditions upon which Figure A.1 data was based.

# LASER ENERGY VS. HV SETTING

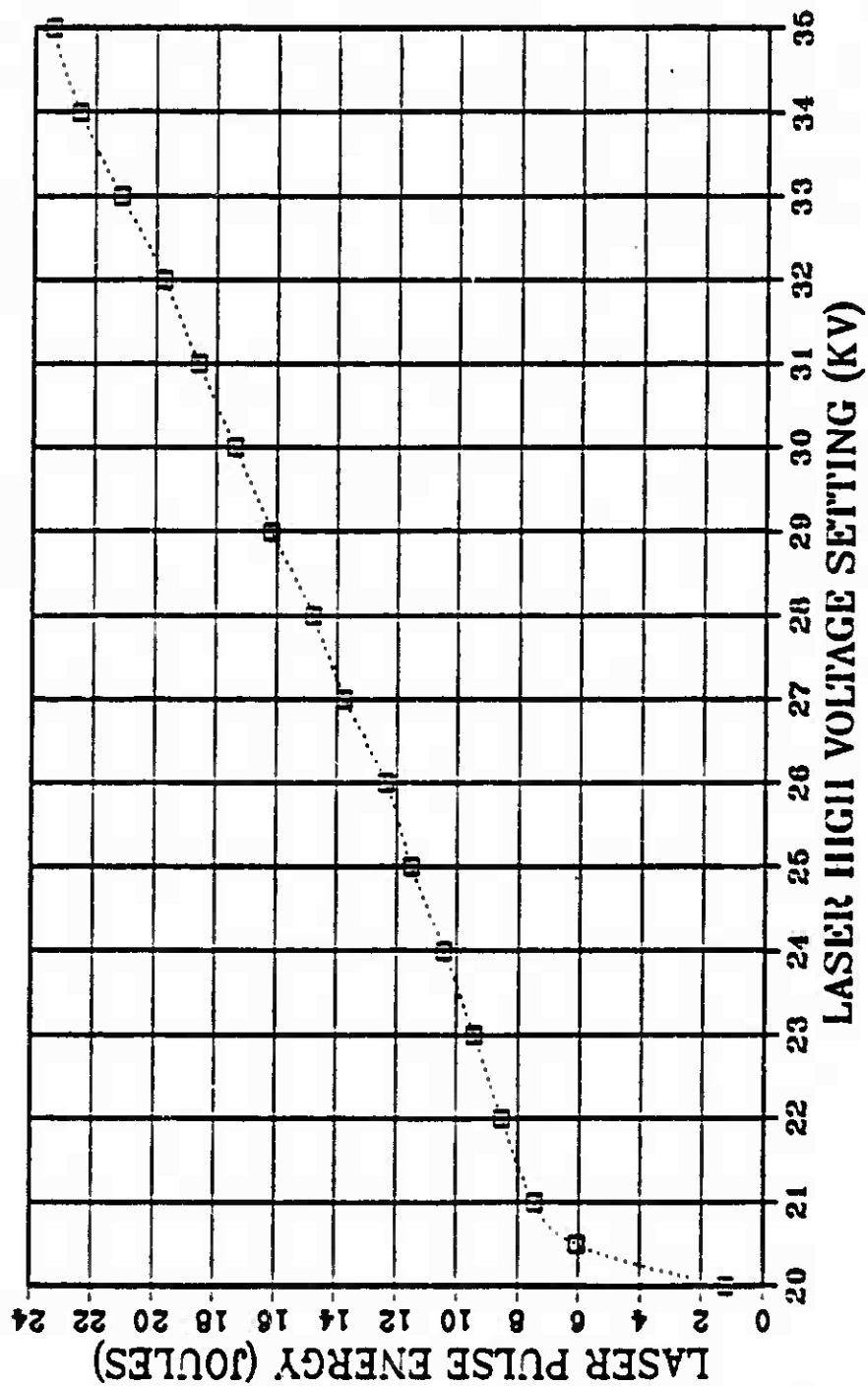


Figure A.1 Laser Pulse Energy Content Versus Laser Power Supply High Voltage Level.

# **APPENDIX B** **TABLES**

**TABLE 1**  
**LASER PULSE ENERGY REPEATABILITY (27 KV/7100 ENERGY METER)**

<i>AIR GAP</i> (psi/SCFH)	<i>NITROGEN</i> (psi/SCFH)	<i>HELIUM</i> (psi/SCFH)	<i>CARBON DIOXIDE</i> (psi/SCFH)
18/6	10/8	10/4	10/8

<i>Laser Shot Number</i>	<i>Energy Meter Reading ( <math>\times 10^{-2}</math> Joules)</i>	<i>Pulse Energy (Joules)</i>
1	1.604	12.34
2	1.621	12.47
3	1.644	12.65
4	1.637	12.59
5	1.648	12.68
6	1.593	12.25
7	1.660	12.77
8	1.597	12.28
9	1.633	12.79
10	1.663	12.79

**MEAN = 1.630**

**12.54**

**STANDARD DEVIATION = 0.024**

**0.186**

TABLE 2  
LASER PULSE ENERGY REPEATABILITY (27 KV/3232 ENERGY METER)

<i>AIR GAP</i> (psi/SCFH)	<i>NITROGEN</i> (psi/SCFH)	<i>HELIUM</i> (psi/SCFH)	<i>CARBON DIOXIDE</i> (psi/SCFH)
18/6	10/8	10/4	10/8

<i>Laser Shot Number</i>	<i>Energy Meter Reading ( <math>\times 10^{-2}</math> Joules)</i>	<i>Pulse Energy (Joules)</i>
1	1.64	12.62
2	1.60	12.31
3	1.65	12.69
4	1.67	12.85
5	1.68	12.92
6	1.71	13.15
7	1.60	12.31
8	1.66	12.77
9	1.67	12.85
10	1.65	12.69

MEAN = 1.653

12.72

STANDARD DEVIATION = 0.032

0.247

TABLE 3  
LASER PULSE ENERGY REPEATABILITY (28 KV/7100 ENERGY METER)

<i>AIR GAP</i> (psi/SCFH)	<i>NITROGEN</i> (psi/SCFH)	<i>HELIUM</i> (psi/SCFH)	<i>CARBON DIOXIDE</i> (psi/SCFH)
18/6	10/8	10/4	10/8

<i>Laser Shot Number</i>	<i>Energy Meter Reading ( <math>\times 10^{-2}</math> Joules)</i>	<i>Pulse Energy (Joules)</i>
1	1.732	13.32
2	1.807	13.90
3	1.741	13.39
4	1.727	13.28
5	1.734	13.34
6	1.759	13.53
7	1.729	13.30
8	1.754	13.49
9	1.771	13.62
10	1.800	13.85
MEAN = 1.755		13.50
STANDARD DEVIATION = 0.028		0.214

**TABLE 4**  
**LASER PULSE ENERGY REPEATABILITY (28 KV/7100 ENERGY METER)**

<i>AIR GAP</i> (psi/SCFH)	<i>NITROGEN</i> (psi/SCFH)	<i>HELIUM</i> (psi/SCFH)	<i>CARBON DIOXIDE</i> (psi/SCFH)
18/4	10/8	10/6	10/8

<i>Laser Shot Number</i>	<i>Energy Meter Reading ( <math>\times 10^{-2}</math> Joules)</i>	<i>Pulse Energy (Joules)</i>
1	1.735	13.35
2	1.796	13.82
3	1.722	13.25
4	1.755	13.50
5	1.757	13.52
6	1.781	13.70
7	1.742	13.40
8	1.759	13.53
9	1.783	13.72
10	1.730	13.31
MEAN = 1.756		13.51
STANDARD DEVIATION = 0.023		0.179

**TABLE 5**  
**LASER PULSE ENERGY REPEATABILITY (33 KV/7100 ENERGY METER)**

<i>AIR GAP</i> (psi/SCFH)	<i>NITROGEN</i> (psi/SCFH)	<i>HELIUM</i> (psi/SCFH)	<i>CARBON DIOXIDE</i> (psi/SCFH)
18/4	10/8	10/6	10/8

<i>Laser Shot Number</i>	<i>Energy Meter Reading ( <math>\times 10^{-2}</math> Joules)</i>	<i>Pulse Energy (Joules)</i>
1	2.501	19.24
2	2.574	19.80
3	2.537	19.52
4	2.497	19.21
5	2.566	19.74

<b>MEAN = 2.535</b>	<b>19.50</b>
---------------------	--------------

<b>STANDARD DEVIATION = 0.032</b>	<b>0.245</b>
-----------------------------------	--------------

TABLE 6  
ONSET OF PLASMA FORMATION DATA FOR SS304 TARGETS IRRADIATED  
IN ATMOSPHERE

<i>Target No.</i>	<i>P<sub>d</sub>(MW/cm<sup>2</sup>)</i>	<i>Plasma Indicated</i>	<i>Arcing Damage</i>
1	1.468	YES	YES
2	1.506	YES	YES
3	2.204	YES	YES
4	1.592	YES	YES
5	1.522	YES	YES
6	0.294	NO	NO
7	0.310	NO	NO
8	0.162	NO	NO
9	0.086	NO	NO
10	0.071	NO	NO
11	0.061	NO	NO
12	0.051	NO	NO
13	0.527	NO	NO
14	0.728	VERY DIM	NO
15	0.652	VERY DIM	NO
16	0.954	YES	YES
17	1.154	YES	YES
18	1.578	YES	YES
19	1.421	YES	YES
20	0.789	DIM	NO
21	0.901	YES	YES
22	0.947	YES	YES
23	0.918	YES	YES
24	0.917	YES	YES
25	0.885	YES	YES
26	0.884	DIM	YES
27	0.844	DIM	NO

TABLE 7  
ONSET OF PLASMA FORMATION DATA FOR SS304 TARGETS  
IRRADIATED IN A VACUUM

<i>Target No.</i>	<i>P<sub>d</sub>(MW/cm<sup>2</sup>)</i>	<i>Plasma Indicated</i>	<i>Arcing Damage</i>
28	0.367	NO	NO
29	0.401	NO	NO
30	0.955	YES	YES
31	1.193	YES	YES
32	1.269	YES	YES
33	1.362	YES	YES
34	1.115	YES	YES
35	1.008	YES	YES
36	1.021	YES	YES
37	0.946	YES	YES
38	0.911	YES	YES
39	0.879	YES	YES
40	0.859	YES	YES
41	0.846	YES	YES
42	0.764	YES	YES
43	0.699	YES	YES
44	0.633	YES	YES
45	0.480	DIM	YES
46	0.427	NO	NO
47	0.467	DIM	YES
48	0.485	DIM	YES
49	0.528	DIM	YES
50	0.460	DIM	YES
51	0.442	VERY DIM	YES
52	0.450	DIM	YES
53	0.452	DIM	YES
54	0.434	VERY DIM	NO

## LIST OF REFERENCES

1. Brooks, K. M., *An Investigation of Early Disturbances Found in Association with Laser-Produced Plasmas*, M.S. Thesis, Naval Postgraduate School, Monterey, California, December 1973.
2. Case, R. S., *An Investigation of Self-Generated Magnetic Fields and Electron Emission in Laser-Produced Plasmas*, Ph.d Thesis, Naval Postgraduate School, Monterey, California, March 1974.
3. Polk, J. S., *Laser Induced Desorption of Gas from Stainless Steel Surfaces*, M.S. Thesis, Naval Postgraduate School, Monterey, California, June 1977.
4. Hwang, Z. W., *Laser Induced Evaporation from Stainless Steel Surfaces*, M.S. Thesis, Naval Postgraduate School, Monterey, California, December 1978.
5. Keville, M. T. and Lautrup, R. W., *An Investigation of Unipolar Arcing Damage on Stainless Steel and TiC Coated Surfaces*, M.S. Thesis, Naval Postgraduate School, Monterey, California, June 1980.
6. Ryan, F. T. and Shedd, S. T., *A Study of the Unipolar Arcing Damage Mechanism on Selected Conductors and Semiconductors*, M.S. Thesis, Naval Postgraduate School, Monterey, California, June 1981.
7. Hoover, T. J., *An Investigation of Unipolar Arcing in Various Conductors and Metallic Glasses*, M.S. Thesis, Naval Postgraduate School, Monterey, California, September 1981.
8. Beelby, M. H. and Ulrich, H. G., *A Study of the Breakdown Mechanism of AISI 304 SS, AISI 2024 Aluminum and Various Titanium Coatings*, M.S. Thesis, Naval Postgraduate School, Monterey, California, December 1981.
9. Metheny, R. M., *An Investigation of Energy Coupling in Various Arc Susceptible and Resistant Conductors*, M.S. Thesis, Naval Postgraduate School, Monterey, California, June 1982.
10. Jenkins, W. F. and Schnidt, W. R., *Thermal Coupling and Damage Mechanisms of 1.06 Micron Laser Radiation and Laser Produced Plasma on Selected Materials*, M.S. Thesis, Naval Postgraduate School, Monterey, California, December 1982.
11. Stephenson, C. O., *Laser Damage to Spherical Targets*, M.S. Thesis, Naval Postgraduate School, Monterey, California, June 1985.
12. Schwirzke, F. and Taylor, R. J., "Surface Damage by Sheath Effects and Unipolar Arcs," *Journal of Nuclear Materials*, v. 93 and 94, pp. 780-784, 1980.
13. Weston, R. L., *CO<sub>2</sub> Pulsed Laser Damage Mechanisms and Assessment of Plasma Effects (Focused Beam)*, M.S. Thesis, Naval Postgraduate School, Monterey, California, December 1986.

14. Behrisch, R., "Surface Erosion from Plasma Materials Interaction," *Journal of Nuclear Materials*, v. 85 and 86, pp. 1047-1061, 1979.
15. Ready, J. F., *Industrial Applications of Lasers*, pp. 336-366, Academic Press, 1978.
16. Chen, F. F., *Introduction to Plasma Physics and Controlled Fusion*, 2nd ed., v. 1, Plenum Press, 1984.
17. Robson, A. E. and Thonemann, P. C., "An Arc Maintained on an Isolated Metal Plate Exposed to a Plasma," *Procedural Physics Society*, v. 73, pp. 508-512, 1959.
18. Naval Postgraduate School Report NPS-61-82-002, *Basic Mechanisms that Lead to Laser Target Damage*, by F. Schwirzke, M. H. Beelby, and H. G. Ulrich, 5 October 1981.
19. Naval Postgraduate School Report NPS-61-83-008, *Unipolar Arcing, A Basic Laser Damage Mechanism*, by F. Schwirzke, 5 May 1983.
20. Naval Postgraduate School Report NPS-61-84-004, *Short Pulse Laser and Plasma Surface Interactions*, by F. Schwirzke, 2 April 1984.
21. Book, D. L., "NRL Plasma Formulary," Naval Research Laboratory, 1980.
22. Miller, R. B., *An Introduction to the Physics of Intense Charged Particle Beams*, pp. 31-39, Plenum Press, 1982.
23. Air Force Weapons Laboratory Report AFWL-TR-73-92, *Explosive Electron Emission and the Characteristics of High-Current Electron Flow*, by R. K. Parker, pp. 17-18, February 1974.
24. Halbritter, J., "Dynamical Enhanced Electron Emission and Discharges at Contaminated Surfaces," *Applied Physics A*, v. 39, pp. 49-57, 1986.
25. Lumonics, Inc., *Insiruction Manual, Lumonics TE-820 HP CO<sub>2</sub> Laser*, 1976.
26. Patel, C. K. N., "High-Power Carbon Dioxide Lasers," *Scientific American*, pp. 264-275, August 1968.
27. Cheo, P. K., *Lasers*, v. 3, pp. 170-173, Marcel Dekker, Inc., 1971.
28. Laser Precision Corp., *Rk-3200 Series Pyroelectric Meter Operating Instructions*, IS-323-03, pp. 1-3, July 1976.
29. Laser Precision Corp., *Rj-7100 Series Radiometer and RjP-700 Series Probes Instruction Manual*, IS-700-03, February 1984.
30. Infrared Associates, Inc., *HgCdTe Infrared Detector Instruction Manual*, October 1984.

31. The International Society for Optical Engineering, *The Industrial Laser Annual Handbook*, 1986 edition, v. 629, pp. 38-55, PennWell Publishing Company, 1986.
32. Cambridge Instruments, Ltd., *Stereoscan 200 Scanning Electron Microscope Operating Instructions*, TL 2025-OM, Issue 3, April 1985.
33. Holman J. P., *Experimental Methods for Engineers*, 3rd ed., pp. 44-51, McGraw-Hill Book Company, 1978.

# INITIAL DISTRIBUTION LIST

		No. Copies
1.	Defense Technical Information Center Cameron Station Alexandria, Virginia 22304-6145	2
2.	Library, Code 0142 Naval Postgraduate School Monterey, California 93943-5002	2
3.	Professor F. R. Schwirzke, Code 61Sw Department of Physics Naval Postgraduate School Monterey, California 93943-5000	2
4.	Professor K. E. Woehler, Code 61Wh Department of Physics Naval Postgraduate School Monterey, California 93943-5000	1
5.	Department Chairman Department of Physics, Code 61 Naval Postgraduate School Monterey, California 93943-5000	1
6.	Plasma Physics and Laser Laboratory Spanagel Hall (Bldg. 232, Rm. 27) Naval Postgraduate School Monterey, California 93943-5000	2
7.	Commander John S. Olson SPC-30 Polaris Missile Facility Atlantic Charleston, South Carolina 29408-5700	2
8.	Lieutenant Richard L. Weston Class 97 Surface Warfare Office School Newport, Rhode Island 02841	1
9.	Dr. R. A. Gerber Laser Projects Division 1244 Sandia National Laboratory P.O. Box 5800 Albuquerque, NM 87185	1
10.	Lieutenant Bruce A. Hoselton 2305 Deanna N.E. Albuquerque, NM 87112	1